

Hyperbolic Metamaterials and Metasurfaces: Fundamentals and Applications

Pengcheng Huo, Si Zhang, Yuzhang Liang, Yanqing Lu, and Ting Xu*

Recent advances in nanofabrication and characterization technologies have spurred many breakthroughs in the field of optical metamaterials and metasurfaces that provide novel ways of manipulating light interaction in a well controllable manner. Among these artificial nanostructured materials, 3D bulk hyperbolic metamaterials and 2D planar hyperbolic metasurfaces exhibit ultra-anisotropic electromagnetic responses and lead to dramatic changes for the light propagation behaviors. Here, the dispersions and realizations of hyperbolic media are first briefly discussed. Then, the recent achievements of various optical applications based on hyperbolic metamaterials and metasurfaces, including beam manipulation, super-resolution imaging, spontaneous and thermal emission engineering, ultrasensitive optical sensing, and broadband optical absorption are reviewed. This review provides an overview and vision for the future of hyperbolic media and their potential impact on the development of novel nanophotonic devices and systems.

1. Introduction

Light is an ultimate information carrier with packaging data in a signal of zero mass and unmatched speed. It allows to go about our daily activities and provides us with telecommunications, security, healthcare, and consumer technologies. Because of its importance, the step of exploration of control over light propagation never stops. Optical metamaterials, as a kind of newly emerging artificial materials, have allowed unlimited possibilities in controlling the flow of light and are being used for a large number of novel optical applications.^[1–6] In principle, optical metamaterials are electromagnetic structures engineered on subwavelength scales to have optical properties that are not observed in their constituent materials and may not be found in nature, such as negative index of refraction.^[7–11] Since the beginning of this century, with the advances of nanofabrication and characterization technologies, more and more research interests have been focused on optical metamaterials

and their potential applications in various fields, including optical waveguiding, imaging, ultrasensitive optical sensing, and electromagnetic cloaking.


Among the different types of optical metamaterials proposed and demonstrated to date, there is one class of highly anisotropic metamaterials which exhibit hyperbolic (or indefinite) dispersions, depending on their effective electric tensors (here, we only consider nonmagnetic media with unit magnetic tensors). Such hyperbolic metamaterials (HMMs) have reached the ultra-anisotropic limit of traditional uniaxial crystal and lead to dramatic changes for the light propagation behaviors.^[12–16] Compared with other optical metamaterials, like chiral^[17,18] and split ring resonator-based metamaterials,^[19,20] HMMs have advantages of relative ease of fabrication at optical frequencies, broadband

nonresonant and 3D bulk responses, and flexible wavelength tunability. As a result, HMMs have attracted widespread interest and become a good multifunctional platform for many exotic applications, such as optical negative refraction and light beam steering,^[12,21–28] subdiffraction-limited imaging and nanolithography,^[29–45] spontaneous^[46–70] and thermal emission engineering,^[71–80] ultrasensitive optical, biological, and chemical sensing,^[81–89] omnidirectional and broadband optical absorption.^[90–93]

On the other hand, ultrathin metasurfaces, which comprise a class of planar optical metamaterials with many subwavelength structural units, have attracted much attention due to their ability of locally controlling the phase, amplitude, and polarization of light at the interface between two natural materials.^[94–97] 2D planar metasurfaces have many advantages over bulk metamaterials, including simplifying the fabrication and integration process, reducing energy loss, and being compatible with other photonics devices. In this context, as an efficient surface wave modulation platform, hyperbolic metasurfaces (HMSs) with in-plane hyperbolic dispersions have a potential influence on the development of on-chip planar photonic devices.^[95,98]

In this review, we first discuss the dispersions and realizations of hyperbolic media. Then, we review the recent achievements of various optical applications based on 3D bulk HMMs and 2D planar HMSs. It should be stressed that, although some application scenarios for 3D HMMs and 2D HMSs are analogous, in fact they are not equal to each other because additional constraints will be introduced on the surface wave as the dimensionality degraded, which is accompanied by fancy in-plane

P. Huo, S. Zhang, Dr. Y. Liang, Prof. Y. Lu, Prof. T. Xu
 National Laboratory of Solid State Microstructures
 College of Engineering and Applied Sciences and Collaborative
 Innovation Center of Advanced Microstructures
 Nanjing University
 Nanjing 210093, China
 E-mail: xuting@nju.edu.cn

 The ORCID identification number(s) for the author(s) of this article can be found under <https://doi.org/10.1002/adom.201801616>.

DOI: 10.1002/adom.201801616

phenomena. Finally, we outline the challenges in the area and offer a set of directions for future work. This review is aimed at providing an overview and vision for the potential development of hyperbolic media in novel nanophotonic devices and systems.

2. 3D Bulk Hyperbolic Metamaterials

2.1. Principle of Hyperbolic Metamaterials

HMMs can be considered as uniaxial media with an extremely anisotropic dielectric tensor, and thus one of the principal components of the relative permittivity tensors has opposite sign to the other two principal components, as

$$\hat{\epsilon} = \begin{bmatrix} \epsilon_{xx} & 0 & 0 \\ 0 & \epsilon_{yy} & 0 \\ 0 & 0 & \epsilon_{zz} \end{bmatrix} \quad (1)$$

where the in-plane components $\epsilon_{xx} = \epsilon_{yy} = \epsilon_{\perp}$, the out-of-plane component $\epsilon_{zz} = \epsilon_{\parallel}$, and $\epsilon_{\perp} \cdot \epsilon_{\parallel} < 0$. The subscripts \perp and \parallel indicate components parallel and perpendicular to the anisotropy axis, respectively. In this review, we only consider electric hyperbolic media, thus the relative permeability $\hat{\mu}$ simply reduces to the unit tensor.

Derived from Maxwell's equations, for transverse magnetic (TM) waves, the unique properties of hyperbolic media can be understood by studying the equifrequency surface (EFC), which is given by

$$\frac{k_x^2 + k_y^2}{\epsilon_{\perp}} + \frac{k_z^2}{\epsilon_{\parallel}} = k_0^2 \quad (2)$$

where k_x , k_y , and k_z are, respectively, the x , y , and z components of the wavevector, $k_0 = \omega/c$ is the free-space wavenumber, ω is the wave frequency and c is the speed of light.

Equation (2) represents a hyperboloid with the condition $\epsilon_{\perp} \cdot \epsilon_{\parallel} < 0$, describing an unbounded frequency surface which is distinct to the closed one in isotropic medium. The hyperbolic dispersion indicates that HMMs support the propagation of electromagnetic waves with large wavevectors known as high- k waves, which are typically evanescent in conventional isotropic media, such as air and glass. These high- k states lead to a broadband divergence in the photonic density of states (PDOS) that can be used for spontaneous emission engineering applications.

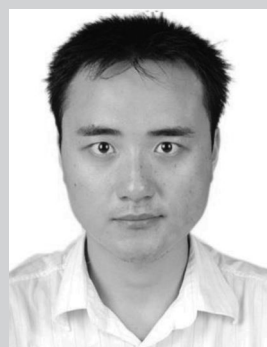
According to the sign of permittivity tensors ϵ_{\perp} and ϵ_{\parallel} , HMMs can be classified into two types. For $\epsilon_{\perp} > 0$ and $\epsilon_{\parallel} < 0$, as shown in Figure 1a, the EFC has a twofold hyperboloid, corresponding to the Type I HMMs. Type I HMMs have relatively low loss because of their predominantly dielectric nature, and they support the propagation of electromagnetic waves with both small and large wavevectors, which can be used for super-resolution imaging. On the other side, for $\epsilon_{\perp} < 0$ and $\epsilon_{\parallel} > 0$, as shown in Figure 1b, the EFC has a onefold hyperboloid, which corresponds to the Type II HMMs. In contrast to Type I HMMs, Type II HMMs exhibit more metallic characteristics and have higher absorption losses. As a result, they only support the propagation of high- k modes and there is a cutoff spatial frequency for the small wavevectors.



Pengcheng Huo is a doctoral candidate student at the National Laboratory of Solid State Microstructures, College of Engineering and Applied Sciences, Nanjing University, China. He received his master's degree in condensed matter physics from the Institute of Solid State Physics, Chinese Academy of Sciences in 2015. His present research mainly focuses on nanophotonics, metamaterials, and metasurfaces.



Si Zhang is a doctoral candidate student at the National Laboratory of Solid State Microstructures, College of Engineering and Applied Sciences, Nanjing University, China. She received her bachelor's degree in materials physics from the Nanjing University in 2015. Her present research mainly focuses on nanophotonics, metamaterials, and metasurfaces.



Ting Xu is a Professor at the National Laboratory of Solid State Microstructures, College of Engineering and Applied Science, Nanjing University, China. He directs an optics laboratory and his group's research includes photonic metamaterials and metasurfaces, nanostructural colors, high-sensitive plasmonic biosensing, and advanced nanofabrication technologies.

2.2. Realizations of Hyperbolic Metamaterials

A few of natural materials have been reported to exhibit hyperbolic dispersion in their original form.^[99–104] For example, graphite is a hyperbolic medium in the wavelength range 240–280 nm.^[101] The crystal structure of magnesium diboride (MgB_2) is quite similar to graphite and the hyperbolic properties appear at the wavelength of 420 nm.^[99] Tetradymites Bi_2Se_3 and Bi_2Te_3 are hyperbolic in the visible range.^[102,103] In the near-infrared (NIR) frequency, ruthenates (Sr_2RuO_4) exhibit hyperbolic electromagnetic responses.^[99] In the far-infrared

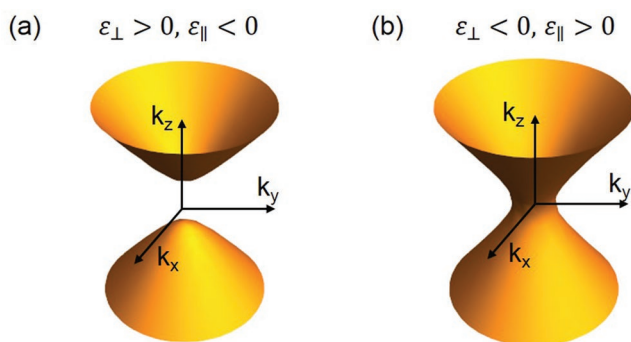


Figure 1. EFC of TM waves in a) Type I and b) Type II hyperbolic metamaterials.

band, the natural hyperbolic materials contain sapphire (Al_2O_3) and bismuth (Bi).^[104] Using first-principle calculations, natural hyperbolic materials are further extended to the broad class of layered transition metal dichalcogenides.^[105] In the homogenous natural hyperbolic materials, the operation wavelength ranges are always fixed and can only be slightly tuned by environmental temperature, pressure, doping, and so on. By contrast, the operational wavelength range of the artificial hyperbolic materials can be flexibly tuned by using different component materials and geometric structures. Therefore, designing artificial metamaterials is the most straightforward way to achieve extraordinary hyperbolic electromagnetic responses at the desired frequencies. In general, there are two prominent approaches to engineering practical optical hyperbolic media. The first one consists of alternating layers of deep-subwavelength thick metal and dielectric (multilayer HMMs), while the second one consists of metal nanowires embedded in a dielectric host (nanowire HMMs). Next, we will discuss these two types of optical HMMs.

2.2.1. Multilayer Hyperbolic Metamaterials

To achieve hyperbolic response, the components of permittivity tensor should be negative in one or two spatial directions. Considering the fact that metal always has negative permittivity below the plasma frequency as the polarization direction of free electron is inverse to the external electric field, negative components of permittivity tensor can be obtained by restricting free-electron motion to these directions. Therefore, the simplest realization of HMMs is multilayer metal–dielectric structures, as shown in **Figure 2a**. According to the effect medium theory (EMT),^[106] the effective permittivity components for propagating perpendicular and parallel to the axis of anisotropy can be calculated as

$$\epsilon_{\perp} = \frac{\epsilon_m t_m + \epsilon_d t_d}{t_m + t_d}, \quad \epsilon_{\parallel} = \frac{t_m + t_d}{t_m/\epsilon_m + t_d/\epsilon_d} \quad (3)$$

where ϵ_m and ϵ_d are the permittivities of metal and dielectric constitutions, t_m and t_d are the thicknesses of metal and dielectric layers. By changing these four parameters, one can get $\epsilon_{\perp} \cdot \epsilon_{\parallel} < 0$ to achieve hyperbolic dispersion. It should be noted here the EMT approximation from Equation (3) only

holds in the long-wavelength limit. In other words, thickness of each layer of HMMs should be far below the size of operating wavelength for the valid homogenization. Considering that the multilayer HMMs are typically fabricated by electron-beam and sputter deposition methods, the minimum metal and dielectric layer thickness should be larger than 5 nm. This layer thickness is much smaller than the operating wavelength of ultraviolet and visible light but still large enough to eliminate additional spatial dispersion in metals induced by quantum size effect, which could guarantee the consistency of electromagnetic responses between designed and fabricated HMMs.

2.2.2. Nanowire Hyperbolic Metamaterials

Besides the alternating metal–dielectric multilayer structure, another approach to achieve behavior is metallic nanowire array embedded in a dielectric host, as shown in **Figure 2b**. When the geometric parameters, including nanowire diameter and lattice period, are much smaller than the operating wavelength, according to EMT approximation, the effective permittivity tensor of the metamaterial can be written in the form of

$$\epsilon_{\perp} = \frac{\epsilon_d [(1+f)\epsilon_m + (1-f)\epsilon_d]}{(1+f)\epsilon_d + (1-f)\epsilon_m}, \quad \epsilon_{\parallel} = f\epsilon_m + (1-f)\epsilon_d \quad (4)$$

where ϵ_m and ϵ_d are the dielectric constants of the metallic nanowire and dielectric host, respectively, and f is the volume filling fraction of metal. As a result, for nanowire structures, we can use these three parameters to tune the metamaterial's dispersion. As most of nanowire HMMs have extremely high aspect ratios (HMM slab thickness approximately several to several tens of micrometers vs nanowire diameter approximately several tens of nanometers), they are always fabricated by electrochemical deposition method, such as growing Ag or Au nanowires inside a self-assembled porous alumina membrane.^[107] Compared with other nanofabrication technology, like e-beam lithography, this is a very efficient and low-cost approach, which allows fabricated metamaterial area to reach centimeter scale.^[28] To get uniform nanowire HMMs, a multistep controlled electrodeposition is necessary to ensure that the metal nanowire filling is consistent over the entire sample area. The overfilling metal nanowires on top of the metamaterial surface can be removed by chemical–mechanical polishing technology.

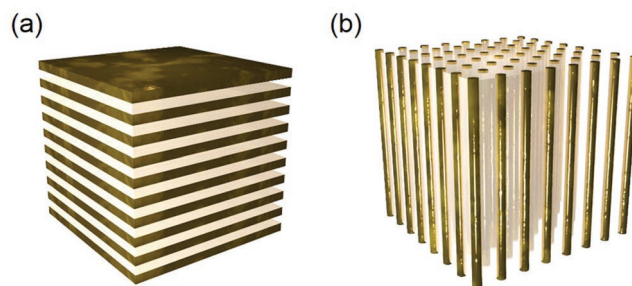


Figure 2. HMMs fabricated in a) multilayer and b) nanowire structures.

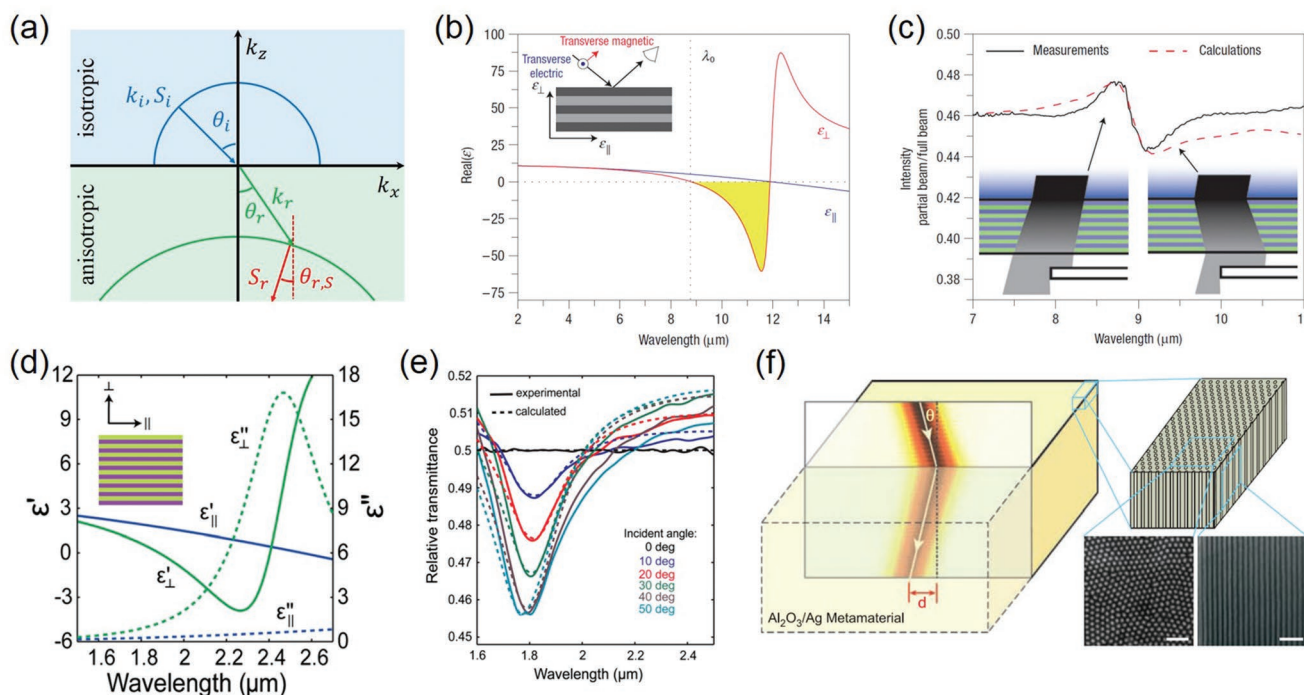


Figure 3. a) Schematic of negative refraction of TM light incident from isotropic to hyperbolic material. b) Dielectric dispersion of a metamaterial consisting of highly doped InGaAs and intrinsic AlInAs layers. c) Spectra of ratio between a partially blocked beam and an unblocked one. The dip of curve indicated the wavelength range of negative refraction. Reproduced with permission.^[23] Copyright 2007, Springer Nature. d) Dielectric dispersion of a metamaterial consisting of AZO and ZnO layers. e) Spectra of ratio between practically blocked and unblocked beam incident from different directions. Reproduced with permission.^[25] Copyright 2012, National Academy of Sciences. f) (left) Schematic of negative refraction from free space into the Ag nanowire HMMs. (right) Schematic of model with nanowires embedding in an AAO templet, and SEM images of sample. Reproduced with permission.^[24] Copyright 2008, American Association for the Advancement of Science.

2.2.3. Material Choice for Hyperbolic Metamaterials

The choice of material combination for HMMs mainly depends on the operation spectral range. For UV light, Ag and Al are the ideal choices of metal due to their low losses. Considering impedance match with real part of permittivity of metal, the dielectric can be poorly absorbing UV transparent materials such as Al_2O_3 .^[30] For visible light, besides Ag and Al, Au is also a good low loss choice for metal. The corresponding dielectric can be SiO_2 ,^[39] TiO_2 ,^[108] Ti_3O_5 ,^[31] MgF_2 ,^[109] polymethyl methacrylate (PMMA),^[47] Si,^[50] and Ge.^[110] For infrared light, convectional plasmonic metals are not suitable for being metal constitutions for HMMs because they have high-impedance mismatch with surround media, which leads to extremely high reflection. Some oxide and nitride-based alloys, such as indium tin oxide (ITO)^[5,111] and AlN,^[112] can be alternative plasmonic metal for the near-infrared light. For mid-infrared light, doped semiconductors InGaAs^[23] and phonon-polaritonic metals (SiC)^[113] can act as the metallic building block.

2.3. Applications of Hyperbolic Metamaterials

2.3.1. Light Beam Manipulation

The special hyperbolic dispersion structure of HMMs brings a lot of convenience to light beam manipulation. The first

widely discussed phenomenon of HMMs is optical negative refraction.^[21,22] Figure 3a schematically shows how optical negative refraction can be obtained at the interface between isotropic material and anisotropic HMMs, where the incident beam and refracted beam are located at the same side of normal. The optical negative refraction can be explained by the EFC of isotropic medium and anisotropic Type 1 HMMs. Here, we only consider TM-polarized light and the electric field and the wavevector, respectively, lie in the x - z plane and the interface lies in x - y plane. In the isotropic material, the circular EFC forces the wavevector k and the Poynting vector S being collinear. At the interface, the conservation of the tangential component k_x indicates that there are two possible solutions in the HMMs. However, the causality principle restricts that $z \cdot S_r > 0$ and thus only the solid blue arrow is reasonable, which implies the wavevector k , indicating the direction of the wavefront propagation, has a positive refraction at the material interface. At the same time, the horizontal component of refracted Poynting vector, written as $x \cdot S_r = k_x H_0^2 / 2\epsilon_z \omega \epsilon_0$, has a negative value because ϵ_z is a negative value. As a result, the optical negative refraction is obtained at the material interface. It should be noted that the above-described effect of optical negative refraction only refers to energy negative refraction when light beam is passing from isotropic medium to HMMs, different from the case of isotropic left-handed metamaterials, in which both phase and energy are negatively refracted and their propagation directions are antiparallel.^[9,114]

Several experiments about negative refraction have been demonstrated in different frequency ranges.^[23–25] For example, in the infrared region, a low loss semiconductor HMMs is demonstrated to exhibit full angle negative refraction effect as in Figure 3b. This metamaterial consists of alternating 80 nm thick semiconductor layers of highly doped InGaAs ($\text{In}_{0.53}\text{Ga}_{0.47}\text{As}$) and intrinsic AlInAs ($\text{Al}_{0.48}\text{In}_{0.52}\text{As}$), which are grown by molecular beam epitaxy on lattice matched InP substrate.^[23] Using reflection and transmission measurements, the ratio of blocked beam to a full beam exhibits a dip, as shown in Figure 3c, which suggests the broadband negative refraction effect in the long wave infrared region. In the near-infrared wavelength range, Naik et al. proposed and experimentally demonstrated a low-loss HMM formed with alternating layers of aluminum-doped zinc oxide (AZO) (60 nm) and ZnO (60 nm) as metallic and dielectric components, respectively (Figure 3d).^[25] As an aluminum-doped zinc oxide, AZO shows that the loss is above 5 times lower than that of Ag in the near-infrared band, which can enable high performance device. The permittivity is positive in the plane and negative out of the plane at wavelength ranging from 1.84 to 2.4 μm , and thus leading to a transverse-positive hyperbolic dispersion. In Figure 3e, the obvious dip in the spectra of ratio of transmittance provides sufficient proof for negative refraction of the corresponding wavelength. At visible frequencies, optical negative refraction has been experimentally observed in bulk HMMs composed of electrochemically deposited Ag nanowires with a subwavelength period,^[24] as shown in Figure 3f. The silver nanowire HMMs can be considered as an effective medium with permittivity in different signs parallel and perpendicular to the nanowires. For the visible wavelength ranging from 660 to 780 nm, the nanowire HMMs exhibit all-angle negative refraction with low-loss intensity decay rate about $\approx 0.43 \mu\text{m}^{-1}$.

Unlike isotropic medium, the propagation directions of group velocities are different with the phase velocities in HMMs, which is dominated by the principle axes of HMMs. Therefore, the planar HMM slabs can be used to achieve refocusing, but it is actually partial focusing: at small angles of incidence, the light rays will be focused a point by the planar slab, whereas the focusing is imperfect and aplanatic point cannot be achieved at large angles of incidence. This effect have been verified with both the ray-tracing argument and the full wave numerical simulation.^[115] Partial focusing guarantees that the HMM slab has great potential to realize lens function. Furthermore, the aplanatic point can be achieved with the present hyperbolic medium by contouring the front and back surfaces of slab, while the actual implementation process is complicated by the finite unit cell size of the structure.

Another related study of light beam manipulation by HMMs is angular optical transparency,^[26,28] which has been demonstrated with several angularly filtering systems, like photonic crystals,^[116,117] plasmonic nanogratings,^[118,119] and geometrical optics.^[120] However, the drawbacks of relatively large angular transparency window and complex architecture hinder their use in practical applications. To overcome these challenges, a single-layer planar architecture based on HMMs has been proposed to achieve narrow optical angular

filtering effect in the visible spectrum.^[28] The basic principle is associated with photonic topological transition (PTT) in metamaterials: via adjusting the permittivity, the metamaterial's EFC can be gradually transformed into hyperbolic topology from elliptical topology. Near the critical point of PTT, the special dispersion topology leads to a narrow optical angle filtering effect. In brief, the incident light beam in all directions is not allowed to transmit through the special material efficiently except in the normal direction, and the schematic diagram of optical angular filtering is shown in Figure 4a. The large-area HMM membrane is shown in Figure 4b, which is fabricated with electrochemical growth of silver nanowires in highly periodic nanoporous anodic aluminum oxide templates synthesized by two step anodization method. The nanopore of the template has a radius of 12 nm and a period of 65 nm. When the light beam transmits through the HMM membrane along the normal direction, the transmission spot is very intense and will darken rapidly with the increase of incident angle, as shown in Figure 4c. The synthetic HMM membrane shows an excellent optical angular filtering performance. In fact, this excellent performance is very suitable to eliminate the interference and diffraction of light in 2D projection imaging, the detailed results are shown in Figure 4d. By covering the 2D aperture with the synthetic HMM membrane, a clear image of object can be projected up to 10 μm away due to suppressing the interference and diffraction of light beam. In the control experiment, the projection distance of the 2D aperture contour is only about 3 μm because there is no angular filter film to eliminate the diffraction. The above results demonstrate that the narrow optical angular filter film (synthetic HMM membrane) can be used to improve the quality of lensless imaging.

The above metamaterials for controlling light beam propagation are all based on Type I HMM. For Type II HMMs, Xu and Lezec fabricated a flat metamaterial-based device at wavelength scale that allows asymmetric transmission of normal incident TM-polarized light in visible frequency range.^[27] As shown in Figure 5a, the proposed device is designed as a sandwich structure with a HMM film composed of alternating Ag (30 nm) and SiO_2 (25 nm) layers in the middle, and parallel metal gratings with different subwavelength periods on both sides (grating A and grating B). According to EMT approximation, the metamaterial is governed by a Type II hyperbolic EFC (Figure 5b), where light incident at any directions from vacuum is unable to transmit but propagate as grating-coupled modes within the material. In addition, the supported modes are contained in a narrow frequency band with wavenumbers larger than the magnitude of the free space wavenumber k_0 . As a result, the gratings A and B can be designed to selectively couple incident light into propagation modes inside HMMs and realize asymmetric optical transmission. Figure 5c is scanning electron microscopy (SEM) image of fabricated sample, cross-sectioned by focused-ion-beam (FIB) milling to observe the inner metamaterial structure. To realize asymmetric optical transmission broadband, there exhibits devices designed at central working wavelength of 532 and 633 nm and both showing valid asymmetric transmission contrast ratios over 14 dB. The proposed reciprocal asymmetric transmission device is promising to be integrated in compact optical systems due to ultrathin planar structure, small capsulation, as well as passive operation.

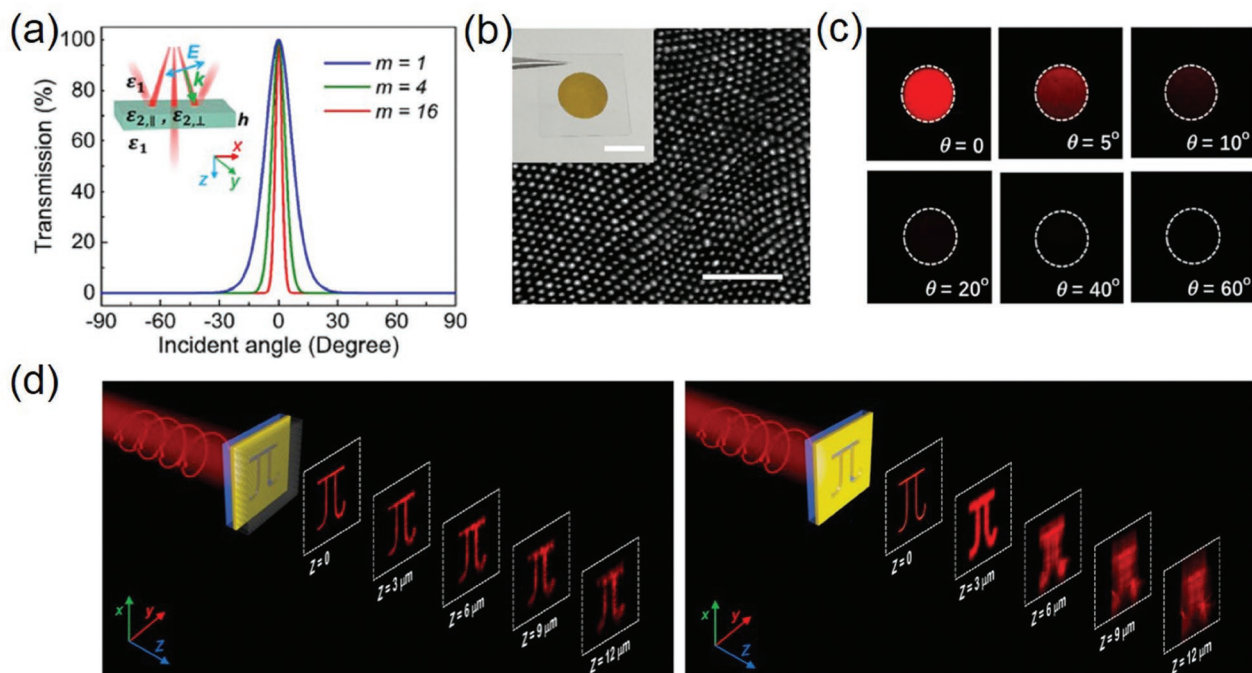


Figure 4. a) Calculated angle-dependent transmission for HMM membrane with different thicknesses. Inset: schematic diagram of the angular filtering. b) SEM image of the fabricated HMM membrane. Scale bar, 500 nm. Inset: large-scale HMM membrane transferred to the SiO_2 substrate. Scale bar: 2 cm. c) Recorded intensity distribution of the transmission spot of TM-polarized light transmitted through the HMM membrane with different angles at $\lambda = 665$ nm. d) Projection imaging of 2D object (left) with (right) without metamaterial. Reproduced with permission.^[28] Copyright 2018, Wiley-VCH.

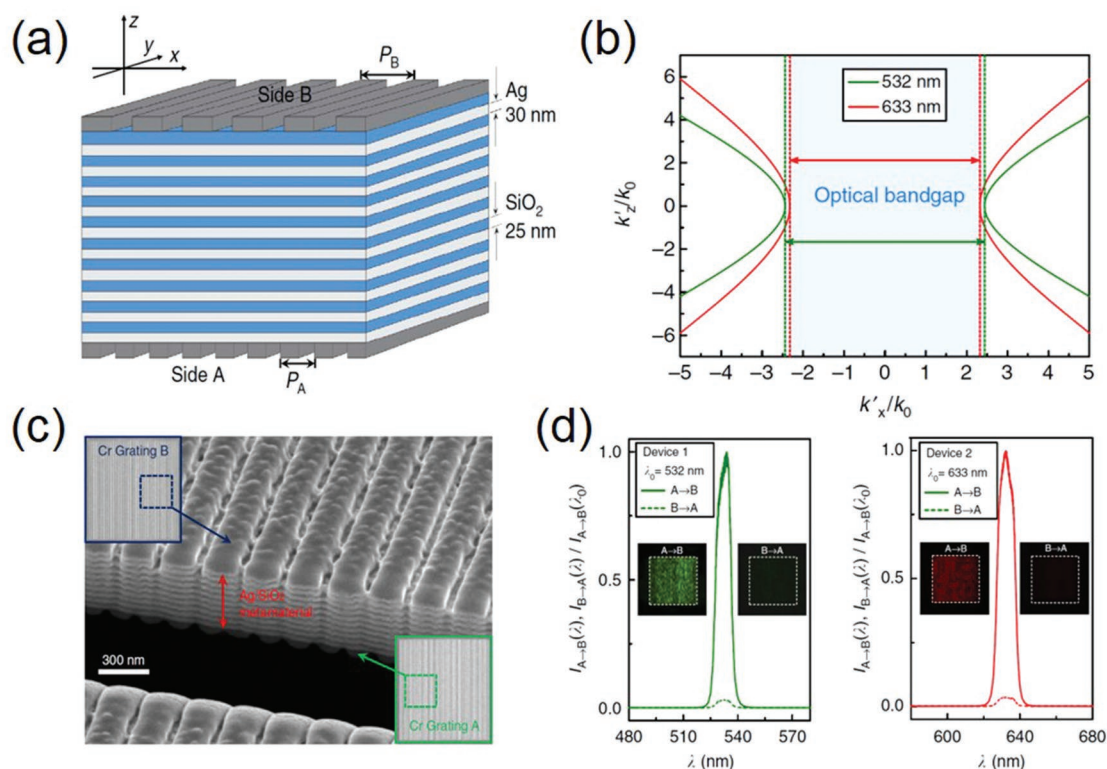


Figure 5. a) Schematic diagram of the Ag/ SiO_2 HMM devices. b) Dispersion relations for the Ag/ SiO_2 HMM for TM polarization. c) SEM image of fabricated experimental device, cross-section reveals the internal multilayers structure. Left inset, SEM image of top Cr grating with 280 nm periodicity. Right inset, SEM image of bottom Cr grating with 200 nm periodicity. d) Experimental forward and backward transmittances for device at $\lambda = 532$ and 633 nm. Reproduced with permission.^[27] Copyright 2014, Springer Nature.

2.3.2. Subdiffraction-Limited Optical Imaging

Classical lens imaging systems exist resolution limitation about half wavelength of light. This obstacle can be understood more profoundly as follows: the scattering light from objects comprises both low spatial frequency propagating components and high spatial frequency evanescent components. The low spatial frequency components which carry large feature information can propagate in free space and be collected by a conventional optical imaging system. However, the high spatial frequency evanescent components carrying fine information decay exponentially and cannot reach the far field. Consequently, the evanescent components have no contribution to the final image and the missing information prevents the subwavelength resolution imaging in the traditional lens systems.

HMMs have been proved to support propagating modes with extremely large wavenumbers (in ordinary material, those high- k modes are evanescent wave) due to the unique anisotropic dispersion relations. Therefore, one of the straightforward applications of HMMs is subdiffraction-limited optical imaging. Superlens based on nanowire and multilayer HMMs have been proposed for subwavelength isometric imaging.^[121,122] More fascinating, HMMs can be used to design hyperlenses,^[29] which can build subwavelength resolution image in the far field based on a magnification mechanism. The conventional hyperlens is a

hollow core cylinder of inner radius R_{inner} and outer radius R_{outer} made of a cylindrically anisotropic homogeneous medium. The high wavevectors modes, which carry near-field high spatial frequency information, are radiated by an object placed at the inner boundary. Because optical angular momentum is conserved, the tangential components of wavevectors are squeezed while propagating at the radial direction. The image is transferred along the radial direction and gradually magnified in the process. At the interface, the ultimate image with supported modes is formed and then sent into far field. The resolution of hyperlens is limited by the operating wavelength in device and can be simply estimated by $\Delta \propto (R_{\text{inner}}/R_{\text{outer}})\lambda$.

The hyperlens with subdiffraction-limited imaging resolution has been experimentally investigated by several groups.^[30,31,33] For example, the first experimental demonstration is a 1D hyperlens, which is optimized at ultraviolet wavelength of 365 nm.^[30] The curved hyperlens is composed of alternate layers of Ag (35 nm thick) and Al_2O_3 (35 nm thick) stacked on a quartz substrate designed into a half-cylindrical valley shape, as shown in **Figure 6a**. The intensity cross-section reveals that the ultraviolet hyperlens is able to resolve down to 125 nm line features, thus achieving an imaging resolution about $\lambda_0/3$ (Figure 6b). It is worth noting that the special geometry structure of 1D hyperlens restricts its image magnification function in horizontal direction, which hinders the application

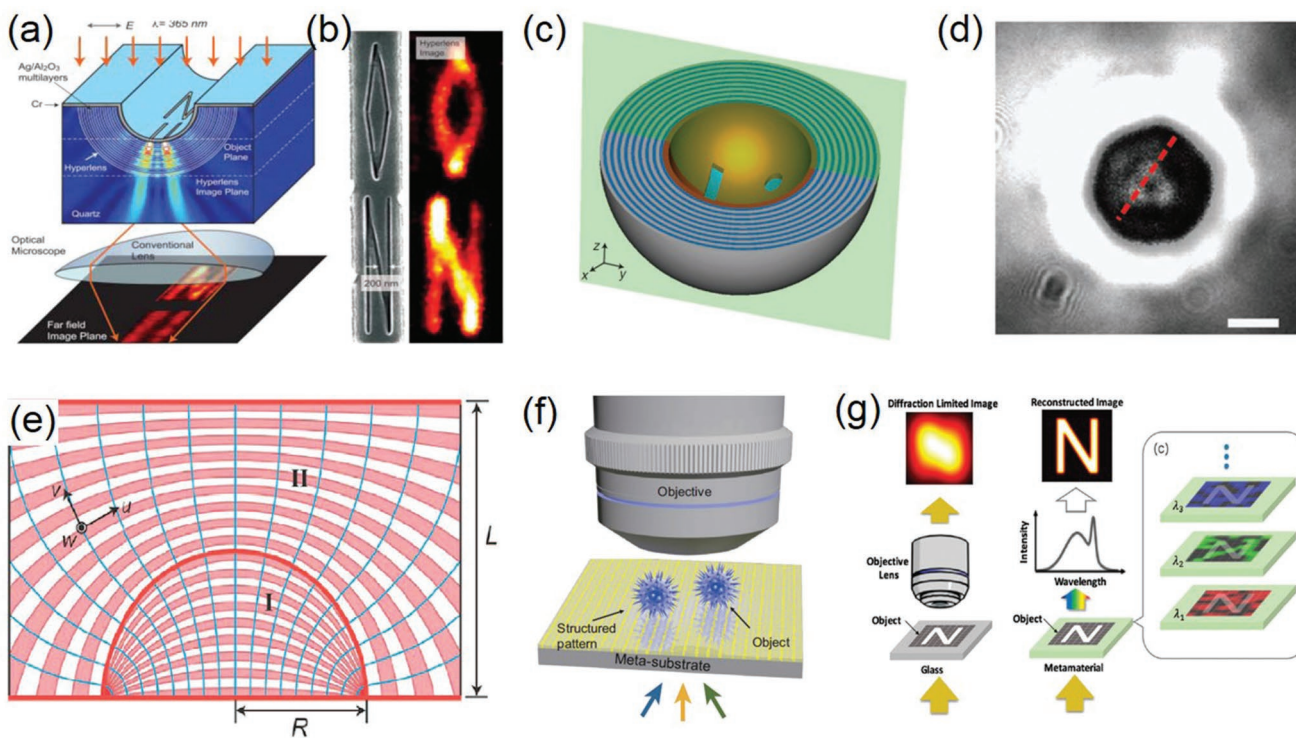


Figure 6. a) Schematic of a cylindrical hyperlens consisting of alternating layers of Ag and Al_2O_3 . The simulation shows a subwavelength imaging of object. b) A pattern with line width of 40 nm imaged with subdiffraction resolution. Reproduced with permission.^[30] Copyright 2007, American Association for the Advancement of Science. c) Schematic of a spherical hyperlens is made of 9 layers of Ag and Ti_3O_5 . d) Subwavelength imaging with the spherical hyperlens. Scale bar is 500 nm. Reproduced with permission.^[31] Copyright 2010, Springer Nature. e) A flat hyperlens designed with transformation optics, which is composed of alternating layers of Ag (pink) and GaN (white). Reproduced with permission.^[124] Copyright 2008, American Chemical Society. f) Schematics of metamaterial-assisted illumination nanoscopy. Reproduced with permission.^[127] Copyright 2018, The Authors, published by Science Press/Oxford University Press. g) The schematic of the compressive spatial-to-spectral transformation microscopy. Reproduced with permission.^[132] Copyright 2017, RSC Publishing.

in many fields. Instead, complete 2D super-resolution imaging can be achieved by spherical hyperlens with magnification directions covering the whole 2D plane. The spherical hyperlens has recently been experimentally demonstrated in the visible frequency range.^[31] The spherical visible hyperlens is arranged in hemisphere geometry with alternating metallic Ag layer (30 nm) and dielectric Ti_2O_3 layer (30 nm) (Figure 6c). Via the hyperlens set up inside a transmission optical microscopy system, the sub-wavelength signals are transferred into propagating modes and later collected by the objective lens. At the incident wavelength of 410 nm, two apertures separated by 160 nm is measured by hyperlens to be 333 nm in the cross-sectional analysis, corresponding to an averaged magnification ratio of 2.08 (Figure 6d).

The original cylindrical and spherical hyperlens discussed above still suffer from some practical problems. For example, the intense anisotropy at the HMM surface brings large impedance, resulting in high reflection and following low efficiency of the system. In addition, structure requirement for a curved geometry hinders the use of ultrathin device in niche applications. To overcome these drawbacks, many studies have been carried out. For the impedance mismatch issue, several possible nonmagnetic designs enforcing impedance matching at the internal interface and external interface have been theoretically proposed,^[123] which can be helpful for significantly suppressing the large reflection loss. In order to replace the inner or outer curved surfaces of hyperlens, the planar structures are considered using concept of transformation optics.^[124–126] On the basis of a flat input surface, the subwavelength near-field signal is transformed into detectable far-field images, then is captured by the traditional detector, as shown in Figure 6e. As another alternative to response these challenges, hyperstructured illumination microscopy (HSIM) has been proposed recently.^[127–129] As shown in Figure 6f, HSIM is based on structured illumination from HMMs, where light beam is incident from the lighting slits at the bottom of the hyperbolic substrate to generate the structured light pattern and the scattering light from the objects is captured by conventional imaging system. For multilayer hyperbolic substrate, the ultimate spatial resolution of HSIM is close to unit cell thickness of metal–dielectric layer pairs, which can be beyond $\lambda/40$.^[130] In practice, due to the fabrication defects, such as structural error and layer thickness fluctuation in multilayer structure, the metamaterial disorders are inevitable. Fortunately, theoretical investigation results show that the influence of nanostructure disorder on the imaging performance is negligible and ultrahigh subwavelength resolution is maintained.^[131] Through transforming the high-resolution spatial information into the spectral domain, 2D super-resolution imaging at visible and infrared wavelength have been demonstrated, as shown in Figure 6g.^[132] The hyperstructured illumination approach combining with the relatively simplicity of planar geometry can offer real-time microscopy without sacrificing in image quality, which would facilitate surface functionalization for cell targeting and bioimaging applications.

2.3.3. High-Resolution Nanolithography

With the rapid development of nanotechnology and increasing demand for fabrication of nanostructures, photolithography

has been propelled and widely used by the integrated circuit industries and semiconductor manufacturing due to the advantages of high resolution and cost-effectiveness. However, the rapidly increasing cost of equipment and complicated photolithography process seriously restrict the further development of semiconductor manufacturing. In addition, the diffraction limit is also an insurmountable obstacle to the resolution of traditional lithography techniques. Although the deep ultraviolet, extreme ultraviolet, or even X-ray lithography with much shorter wavelength are aggressively expected to improve the photolithography resolution, they will drastically increase the instrument complexity and the manufacture cost.

A high-resolution interference photolithography method using HMMs to generate the deep-subwavelength features from the conventional lithographic mask is first proposed by Xu et al.^[34] Due to the strict limitation of the hyperbolic dispersion relation, only the evanescent waves carrying high frequency information can transmit through the HMM filter and interact with the actual photoresist. As shown in Figure 7a, the HMMs consist of multilayers of silver (20 nm) and SiO_2 (30 nm), and the corresponding dispersion relation with a Type II hyperbolic shape only supports the propagation of field components with high spatial frequencies. For a conventional chromium grating with 320 nm periodicity and incident light at a wavelength of 442 nm, the generated interference patterns in the photoresist layers have the feature size about 40 nm, smaller than 1/11 of exposure wavelength (Figure 7b). Furthermore, this approach can even be used to achieve sub-22 nm feature size by redesigning HMMs and reducing the incident wavelength,^[36] as shown in Figure 7c. Here, HMM is a dielectric–metal multilayer structure with 4 pairs of GaN (10 nm) and aluminum (12 nm) multilayer. A photolithography mask of 86 nm pitch and 40 nm thickness chromium grating is illuminated with TM-polarized light at a wavelength of 193 nm. Interference patterns with 21.5 nm feature size are then formed in the photoresist layer, smaller than 1/8 of exposure wavelength.

To advance the understanding of the formation of interference patterns and to increase the pattern contrast and field depth, analysis of the properties of surface plasmon propagation in HMMs has been carried out by treating the metamaterial multilayers as coupled waveguides.^[38] The process of light propagating between the multilayer waveguide and air slits in the chromium mask can be analyzed via the coupled mode theory. When the grating mask of 240 nm pitch is irradiated by light source with wavelength of 193 nm, the characteristic size of the interference pattern can be reduced to 20 nm by optimizing the structural parameters. The corresponding filed depth can reach 40 nm, as more than 2 times larger as the previous one. In addition, the film roughness can distort the normal propagation and coupling of waves especially in nanoscale film, leading to nonuniform photoresist patterns with poor profiles. To design and estimate the photolithography system, the effects of the surface roughness of thin film, line edge roughness, and defects on photomasks are systematically investigated.^[45] The optical transfer function of the HMM system presents a function of spatial frequency selection, which suppresses the impacts of rough surfaces and leads to steady interference with the selected diffracted wave. As a result, even with the surface roughness from metamaterial multilayer, the

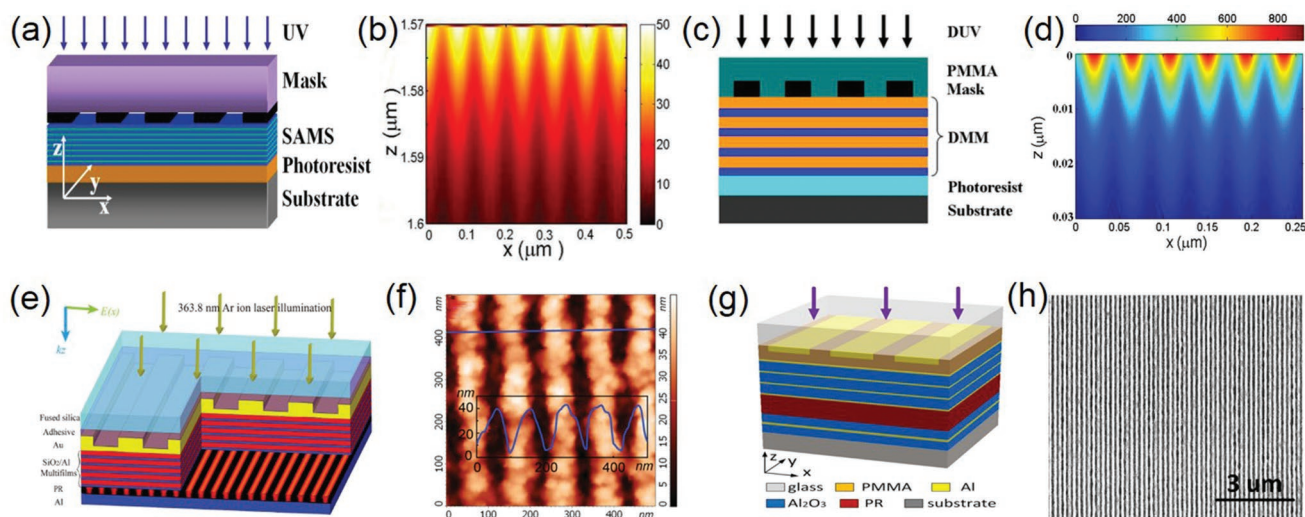


Figure 7. a) Schematic drawing of proposed photolithography assisted by HMM. b) Calculated electrical field distribution for chromium mask with a period of 160 nm. The p-polarization plane waves are vertically incident to chromium masks. Reproduced with permission.^[34] Copyright 2008, OSA Publishing. c) Schematic of plasmonic interference lithography with HMM filter. d) The calculated electric field distribution for mask with periods of 86 nm. Reproduced with permission.^[36] Copyright 2009, OSA Publishing. e) Schematic of two BPP interference structure with HMM. f) Atomic force microscopy (AFM) image of BPP interference photoresist pattern. Reproduced with permission.^[41] Copyright 2015, Wiley-VCH. g) Schematic of the proposed ENZ UV lithography. h) SEM image of the patterns achieved with ENZ lithography. Reproduced with permission.^[44] Copyright 2017, American Chemical Society.

line edge roughness of the pattern imaged by HMMs only increases slightly and the total field intensity is stable.

The deep-subwavelength photolithography technology assisted by HMMs has been experimentally demonstrated in several studies.^[40,41] The detailed schematic diagram is shown in Figure 7e. A TM-polarized plane wave with 363.8 nm wavelength normally incidents on a 1D grating mask from the SiO₂ substrate side. The HMM structure composed of alternatively five stacked pairs of Al/SiO₂ films is placed beneath a Au grating with periodicity of 360 nm. Surface plasmon modes at the interface are excited to generate interference pattern with deep-subwavelength size in a relative broad area of the photoresist. In experiment, the uniform interference patterns with half pitch 45 nm ($\lambda/8$) are achieved (Figure 7f).^[41] Another method to obtain deep-subwavelength feature size is to use an evanescent Bessel beam, which is generated by utilizing HMM multilayers structure, along with the concentric metasurface and plasmonic cavity lens in the form of Ag/photoresist/Ag structure.^[43] Combining the spatial filtering characteristics of HMMs with the electric field modulation of plasmonic cavity, the minimum size of the patterns can be reduced to 62 nm at the operating wavelength of 365 nm.

The approaches assisted by HMMs can produce subdiffraction-limited patterns. However, the huge energy loss inside the HMM multilayers leads to that the electric field intensity interacting with the photoresist is very low, hence the whole process requires a long exposure time.^[38] In response to this challenge, it is advisable to build a lithography system with the ability to produce subwavelength resolution patterns in high transmission. Recently, a deep-subwavelength photolithography configuration is investigated by applying a special epsilon-near-zero (ENZ) HMMs,^[44] as shown in Figure 7g. The system consists of Al grating photomask, PMMA spacer, HMMs for index matching, and photoresist layer successively. In order

to enhance the interaction between the electric field and photoresist, extra Al and Al₂O₃ layers are deposited close to the photoresist layer, accompanied by strong reflection and cavity resonance. The ENZ HMMs composed of alternating Ag and Al₂O₃ layers, which are Type II HMMs with the tangential component of the permittivity closing to zero. The special dispersion relation of ENZ HMMs ensures the horizontal transmission of single plasmonic mode with low energy dissipation. As shown in Figure 7h, for the exposure light at a wavelength of 405 nm, periodic patterns with a half pitch of 58.3 nm are achieved. The recorded patterns are smaller comparing with that in the photomask and keep with high aspect ratio and well uniformity. The line feature size is 1/6 of the photomask with half pitch of 350 nm and about 1/7 of the wavelength of radiation source (405 nm).

In addition to HMM-assisted interference photolithography, the hyperlens can also be used to perform projection lithography just by simply reversing its direction of operation, which is first proposed in 2009.^[37] As shown in Figure 8a, the outside of the hyperlens is covered with a diffraction-limited photomask. The tangential component of wavevectors increases gradually as the light travels radially toward the inner surface of the lens. And thus, the final pattern with subwavelength feature size can be achieved at the output surface. Recently, this proposal has been experimentally demonstrated using a demagnifying hyperlens.^[42] As shown in Figure 8b, there are multilayers of Ag (30 nm) and Ti₃O₅ (30 nm) film pairs stacking on the SiO₂ substrate milled into a cylindrical valley shape. A pre-deposited 50 nm Cr film is etched into photomask with pattern “UB” and line width of 300 nm, as shown in Figure 8c. After the exposure using 405 nm laser source, Figure 8d shows SEM image of the exposed photoresist with a reduced “UB” pattern. The 170 nm line width confirms that the reduction factor of the pattern is about 1.8. A reference sample shows that the pattern

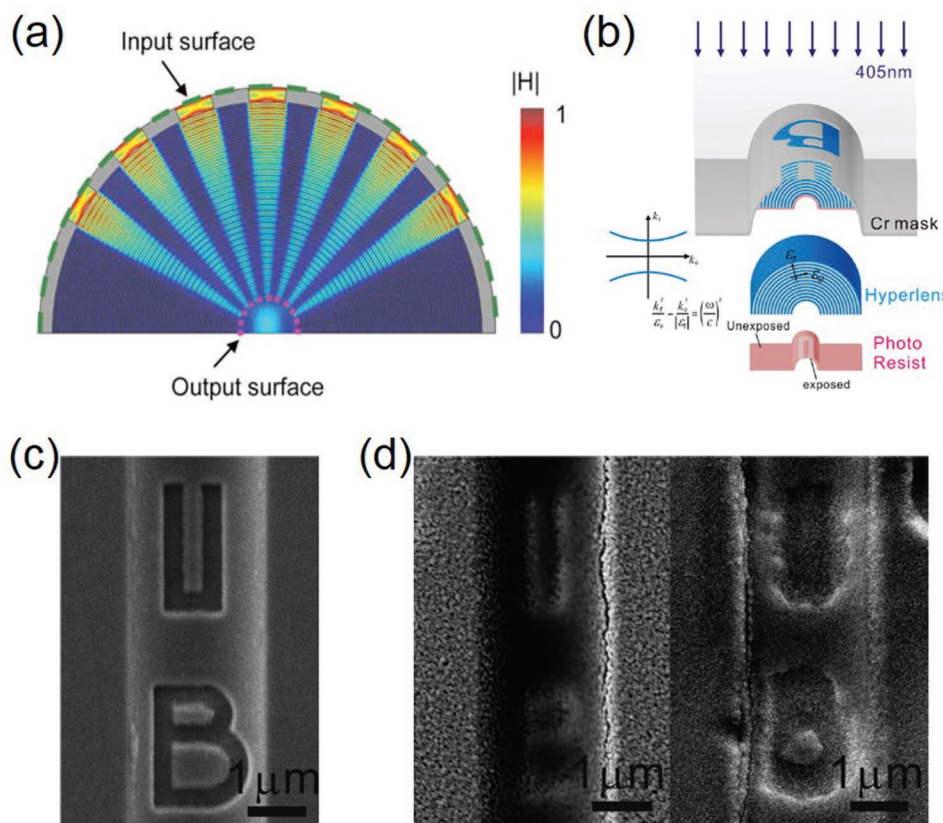


Figure 8. a) A cylindrical hyperlens to generate a 1D subwavelength patterns from a traditional mask. Reproduced with permission.^[37] Copyright 2009, AIP Publishing. b) Schematic of the lithography device with a demagnifying hyperlens. The inset: the hyperbolic dispersion relation of HMM. c) Original “UB” pattern on the Cr mask. d) (left) Recorded pattern on the photoresist using hyperlens. (right) Recorded pattern on the photoresist using magnesium fluoride lens. Reproduced with permission.^[42] Copyright 2016, American Chemical Society.

generated on the output surface of magnesium fluoride lens is rather fuzzy due to the lack of high frequency information. Furthermore, in this method, the inner and outer surfaces of the hyperlens can be artificially processed into arbitrary curvature, which is more useful for practical applications.

2.3.4. Spontaneous Emission Engineering

In a homogeneous lossless medium, the radiative decay rate of an emitter between initial excitation state $|i, 0_k\rangle$ and final state $|f, 1_k\rangle$ is written in^[133]

$$\Gamma_{fi} = \frac{2\pi}{\hbar} \rho(\hbar\omega_k) \left| \langle f, 1_k | H_{int} | i, 0_k \rangle \right|^2 \quad (5)$$

Here, \hbar represents Dirac’s constant, $H_{int} = \mu \cdot E$ represents interaction Hamiltonian operator as the dipole matrix element μ between the two states coupling with the electric field E , and $\rho(\hbar\omega_k)$ is PDOS at transition frequency ω_k . More specifically, $\rho(\hbar\omega_k)$ is the number of available electromagnetic modes for the emitter to radiate into per unit frequency and per unit volume. Therefore, change of surroundings would alter the mode density and further modify the spontaneous emission rate.

Purcell first explored the concept of spontaneous emission modification in a cavity in 1946.^[134] In a cavity where the transition frequency of the emitter is resonant with the fundamental mode, the generally known Purcell factor, which is the ratio between the modified and free-space emission rate, is given by $F_p = \frac{\Gamma_{mod}}{\Gamma_0} = \frac{3Q\lambda^3}{4\pi^2 V_0}$, where λ is the resonant wavelength, Q is the quality factor of the cavity mode, and V_0 is the effective mode volume. It denotes that light tightly confined in small dimensions and stored for a rather long time by resonators will bring an increased emission rate.

Traditional approaches to realize such kind of spontaneous emission modification is to use photonic crystal nanocavities^[135] and plasmonic nanostructures as resonators to trap light.^[136] However, although the material and optical regimes involved in photonic crystals cavities and plasmonic nanostructures are different, their intrinsic emission modification mechanisms both rely on the resonant properties of “cavity” and lead to limited numbers of modified emission modes in a continuous spectrum. HMMs successfully overcome such weakness and can realize a broadband enhancement of spontaneous emission.^[137] In contrast to the isotropic environment, where the EFC is closed in the k -space and leads to finite PDOS, the hyperbolic medium provides an open EFC and large summation area in the k -space and hence a much larger PDOS. Such large number

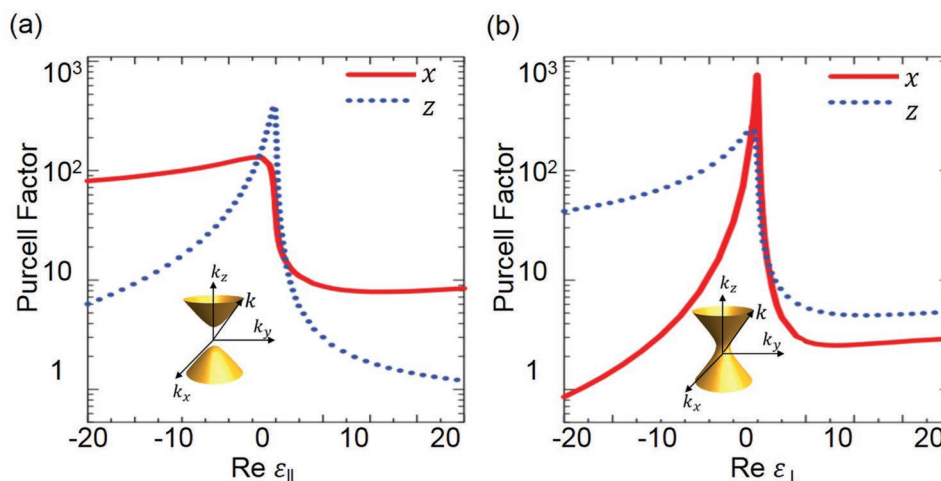


Figure 9. Theoretical Purcell factor of a HMM relative to a) $\epsilon_{||}$ for $\epsilon_{\perp} = 1$ and b) ϵ_{\perp} for $\epsilon_{||} = 1$. Solid and dashed lines represent the x-oriented and z-oriented dipoles, respectively. Inset shows the corresponding EFC in the k -vector space. Reproduced with permission.^[138] Copyright 2012, American Physical Society.

of modes can strongly enhance the emission rate at any frequency with a hyperbolic dispersion, making it possible to achieve the broadband modification in one system. **Figure 9a,b**, respectively, shows the calculated Purcell factors for dipole parallel and perpendicular to the symmetric axis (z -axis) for Type I and Type II HMMs.^[138] It can be clearly seen that the Purcell factor increases when the material regime transits from elliptic to hyperbolic when the dielectric constant $\epsilon_{||}$ (Figure 9a) and ϵ_{\perp} (Figure 9b) change from positive to negative values.

Several experiments have successfully demonstrated the spontaneous emission modification and related applications using HMMs.^[48,51,53,57,64,66,68] For example, **Figure 10a** depicts the dependent relation of the CdSe/ZnS quantum dot lifetime dispersed on the metal-dielectric multilayer structures to emitting wavelength. The metamaterial consists of alternant films of Ag and TiO₂ with different fill fractions of the metal, as shown in the inset of Figure 10a.^[48] Through artificial design, the topology of EFC experiences the transition from the closed (ellipsoid) to the open (hyperboloid) one through the transform wavelength. As a result, for samples with 29% and 33% filling ratios of silver, the normalized lifetime of the emitter is significantly reduced. By contrast, the lifetime of emitter for the 23% silver-filled sample experiences steady variation due to the lack of the transition in topology. These experimental results demonstrate the effect of hyperbolic substrate in spontaneous emission manipulation.

However, due to the limitation of dissipation and large impedance mismatch in bulk HMMs, it has been demonstrated theoretically^[61,70] and experimentally^[50,54–56,59,65,67] that the emission rate and intensity will be higher within the HMMs than near the interface. For example, using nanopatterned Ag–Si multilayer HMMs, the spontaneous recombination rate in InGaN/GaN quantum wells (QWs) can be enhanced to ≈ 160 -fold in broadband.^[67] Figure 10b shows the experimental results and theoretical fit of time-resolved photoluminescence (PL) for the as-grown InGaN QWs, QWs with uniform and patterned HMMs. The nanostructured HMMs outcouple the high- k HMM modes to the far field and increase the emission intensity.

When the central wavelength of emission light is close to the resonant wavelength, the strong interaction between QWs and the patterned HMMs leads to the dramatic Purcell factor enhancement. Besides patterning the HMMs, one can also integrate the emission source into the hyperbolic regime,^[54] as in Figure 10c,d. The GaAs quantum wells are embedded in rolled-up metamaterials, as depicted in the inset of Figure 10c. The lifetime of the QWs in the samples with different silver layer thicknesses is shown in Figure 10c, which is reduced by a factor of 2 with hyperbolic dispersion. And, the finite-difference time-domain (FDTD) simulation results in Figure 10d reveal the different propagation of the emitting mode. Figure 10e shows the fluorophores composited with the nanorod-based hyperbolic regime.^[59] Through the time-resolved PL measurements, a 30 times reduction of macroscopically averaged lifetime in broadband is observed. The local and nonlocal of the process are investigated theoretically and experimentally, which may enable new applications with macroscopic composites.

There have been attempts to realize nanolaser using HMM structures based on the emission enhancement mechanism.^[52,60,62,63] The broadband Purcell enhancement and more efficient energy transfer from the surface plasmon to the lasing mode due to the large PDOS and nonlocal effect in HMMs pave ways to manipulate the lasing action. Figure 10f presents a single-mode deep-ultraviolet plasmonic laser by using a hyperbolic metacavity on a multiple quantum well (MQW).^[63] In the metacavity array composed of nanorod HMMs, all the excited plasmon oscillations can be coupled into one lasing mode. The inset of Figure 10f shows the calculated mode pattern of the (3,1) mode. The radiation flows will propagate from the sidewall of metacavity to the QW, and a part of them then couples back to the metacavity and provides strong feedback. The PL spectrum with different pump powers of the composite system is shown in Figure 10g, where a narrow lasing peak is observed at 289 nm wavelength. With the presence of the hyperbolic metacavity, the emission rate of ultraviolet emitter is enhanced about 33 times. Also, it has been proved that the lasing threshold can be reduced by 35% in

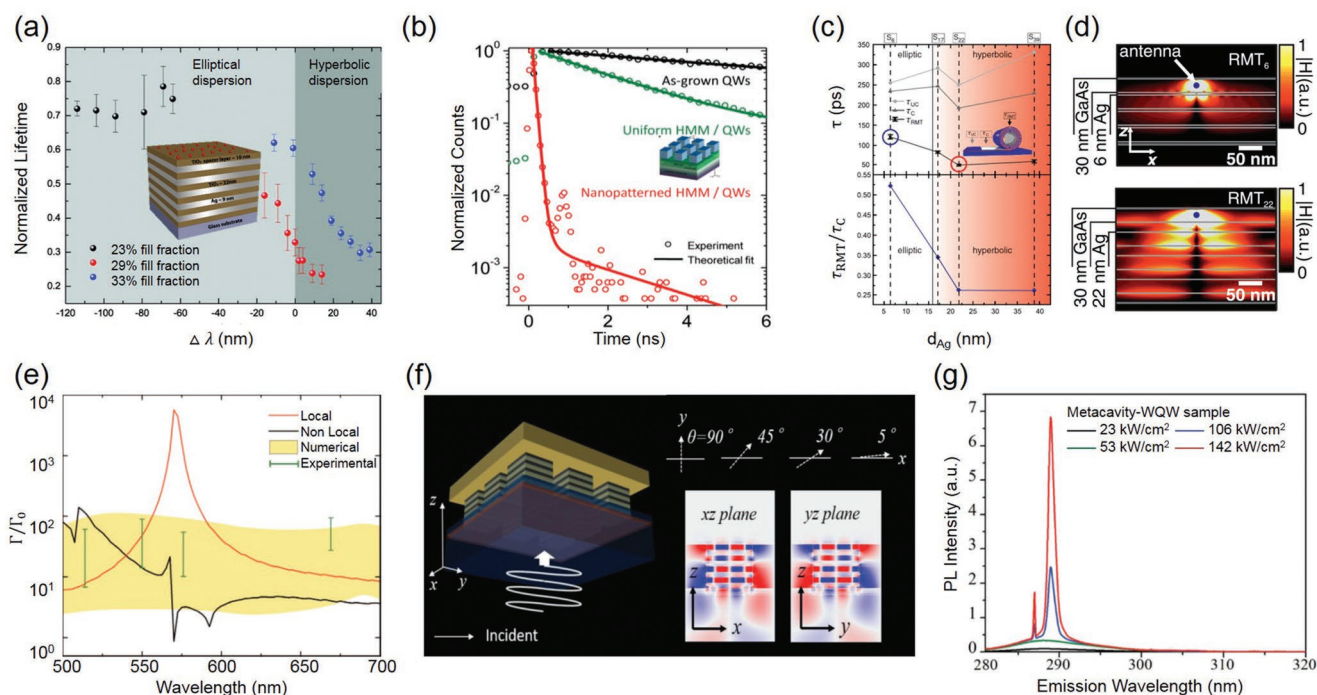


Figure 10. Spontaneous emission modification in HMMs. a) The normalized lifetime of CdSe/ZnS colloidal quantum dots on the surface of metamaterials with Ag/TiO₂ multilayer structures with wavelength. Reproduced with permission.^[48] Copyright 2012, American Association for the Advancement of Science. b) Experimental results and theoretical fit of time-resolved PL spectrum for the as-grown InGaAs QWs (black open circles), QWs with unpatterned Ag-Si multilayer HMMs (green open circles), and with patterned HMMs (red open circles). Reproduced with permission.^[67] Copyright 2018, Wiley-VCH. c) QW lifetimes τ_{UC} (gray dots), τ_c (gray triangles), and τ_{RMT} (black squares) on the samples S_6 , S_{17} , S_{22} , and S_{39} , and normalized lifetime τ_{RMT}/τ_c with the Ag layer thickness d_{Ag} . d) Simulated normalized magnetic field amplitude for a dipole antenna on the top layer of rolled-up microtubes RMT₂₂ and RMT₆. Reproduced with permission.^[54] e) Dependent relation of the emitter lifetime (red) local theory, (black) nonlocal theory, (bars) experimental data of width for the lifetime distribution at 10% modal amplitude. Reproduced with permission under the terms of a Creative Commons Attribution-NonCommercial-NoDerivs 4.0 International License.^[59] Copyright 2017, The Authors. f) The calculated mode pattern of the (3,1) mode using an excitation plane wave with various incident angles. g) PL spectrum with different pump powers. Reproduced with permission.^[63] Copyright 2018, Wiley-VCH.

hyperbolic medium compared to the elliptic one.^[60] The strong enhancement of laser action achieved by HMMs provides an efficient scheme for high-efficiency light-emitting devices.

2.3.5. Ultrasensitive Optical Sensing

The HMMs can be also used as a good platform for realizing high sensitive optical sensing.^[86,87] As mentioned before, HMMs mainly have two typical structural types relied on the negative direction of effective permittivity: metallic nanowire array and metal/dielectric multilayer. Both these two hyperbolic structures have been used to develop high performance biosensors. For example, as shown in **Figure 11a,b**, a biosensor based on 2D gold nanowire arrays is proposed and demonstrated with a sensitivity exceeding 3×10^4 nm per refractive index unit.^[81] This nanowire-based HMM sensor outperforms conditional surface plasmon sensors made of unpatterned metallic films.^[83] However, high sensing properties of the nanowire-based metamaterials relies on the bulk Kretschmann prism configuration, which is not suitable for point-of-care sensing application owing to the affiliated bulky structure. To overcome this drawback, miniaturized plasmonic biosensor platforms based on metal/dielectric multilayer HMMs are proposed based on both wavelength modulation scheme^[84] and angular modulation sensing

scheme,^[85,88] as shown in **Figure 11c,d**, which exhibit extremely high sensitivity from visible to near-infrared wavelength range. The extremely high sensitivity of this HMM biosensor makes it be able to detect small biological molecules (244 Da) at picomole concentrations. In this configuration, the subwavelength grating-coupling structure is used to excite the high order mode in the metal/dielectric multilayer, which makes it possible for designing the miniaturized and multiplexed sensors.

Another hyperbolic chiral-sculptured thin film structure as a highly sensitive sensor is also theoretically investigated.^[88] In the angular modulation sensing scheme, the bulk sensitivity of this hyperbolic plasmonic sensor is up to 6000° per refractive index units of the infiltrating fluid. Such high refractive index sensitivity is attributed to strong near-field enhancement of surface plasmon waves on the interface of a metal and a hyperbolic chiral-sculptured thin film. Besides biosensing application, temperature sensor is also designed based on HMMs using hygroscopic dielectric blend.^[89] This dielectric blend consists of a polymer, a sol-gel unsintered TiO₂, and an organic dye. When such a dielectric blend is embedded in the HMMs, its reversible change of the physical thickness and refractive index induces an ENZ wavelength shift by about 25 nm as the environment temperature changes from room temperature to 80 °C. This remarkable tuning range of ENZ wavelength of HMMs is promising for many applications, such as energy

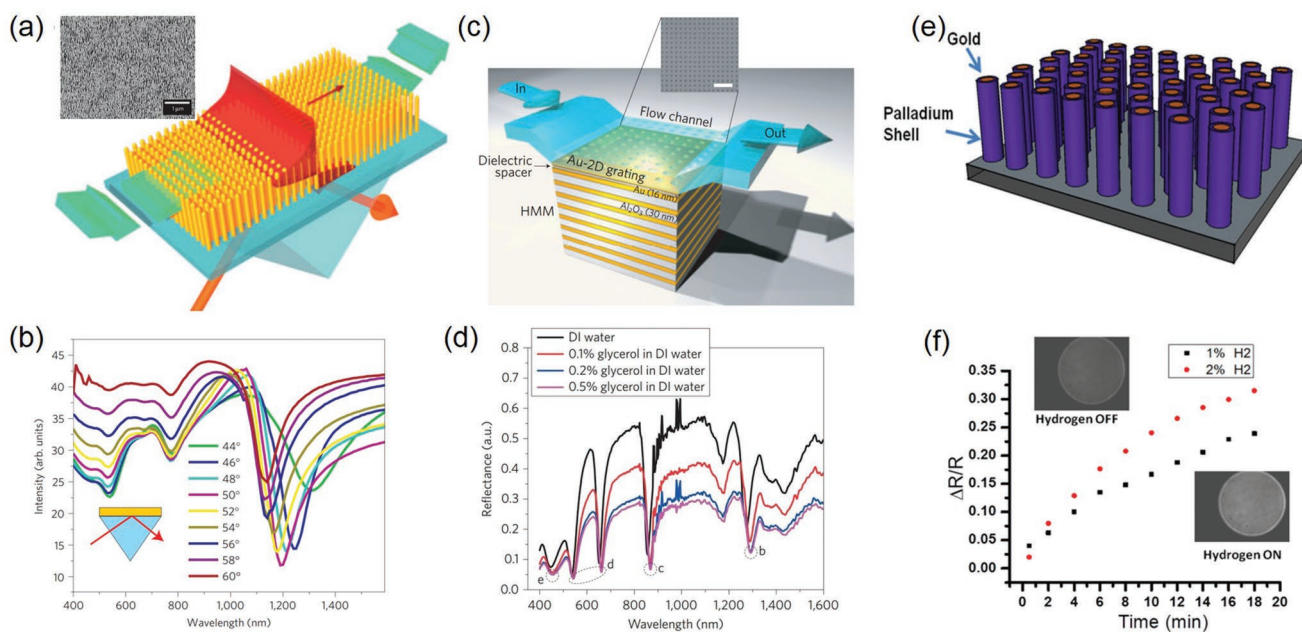


Figure 11. a) Schematic of the nanorod-based HMM sensor. Inset shows SEM image of nanorod arrays. b) Reflection spectra of the nanorod array in the water environment for different incident angles. Reproduced with permission.^[81] Copyright 2009, Springer Nature. c) Schematic of plasmonic biosensor based on metal/dielectric multilayer HMMs. d) Reflection spectra of the sensor device in (c) by injecting different weight percentage concentrations of glycerol in the water environment. Reproduced with permission.^[84] Copyright 2016, Springer Nature. e) Schematic of the hydrogen sensor based on hybrid Au/Pd nanorod array. f) Time-dependent reflectivity for different concentrations of hydrogen. Inset shows photographs of the sensor with and without hydrogen. Reproduced with permission.^[82] Copyright 2014, Wiley-VCH.

squeezing, fine temperature sensing, and so on. Furthermore, the HMMs based on hybrid Au/Pd nanorod array has been used to develop ultrasensitivity hydrogen sensor. The proposed sensor is performed in the Kretschmann configuration where bimetallic (Pd/Au) nanorod-based HMM is attached on the prism,^[82] as shown in Figure 11e,f. The results show distinct shifts in reflection and transmission spectrum when the HMM contacts with 2% hydrogen in nitrogen, implied the ultrahigh sensitivity. Such high sensitivity is a manifestation of the hyperbolic dispersion of the nanorod metamaterials. This HMM hydrogen sensor has great application potential owing to the high efficiency and low-cost fabrication technique. Thus, HMM is promising for ultrasensitive biological and chemical sensors.

2.3.6. Broadband Optical Absorption

In 2008, Landy et al. designed a narrow band metamaterial perfect absorber composed of metallic split ring resonators and cutting wires.^[139] Later on, different schemes have been proposed to improve the performance of the metamaterial absorbers. To create controlled absorption over a broadband, there have been proposals to combine several types of strong resonators.^[140–142] However, if amounts of resonators are crammed into an area, the fabrication procedure becomes more complex and the absorption band barely get broadened. Due to possessing the properties of large PDOS, HMMs have attracted a lot of attention as a candidate for realizing broadband optical absorption. As shown in Figure 12a,b, by

tailoring the multilayer HMMs into sawtooth shape, numerical investigation manifests the outstanding performance of HMM absorber with absorptivity higher than 95% from 3 to 5.5 μm .^[90] This phenomenon of broadband absorption can be understood by slow light modes in HMMs. Microscopically, the absorption process happens with each sawtooth unit acting as an independent metamaterial slow light waveguide to trap and dissipate the light energy. Light of shorter and longer wavelength is trapped by the upper narrow parts and broad bottom of the sawtooth, respectively. Experimental demonstrations of HMM optical absorber in NIR and visible range have been performed by either FIB milling^[91] or nanoimprint method,^[92] as shown in Figure 12c,d.

The absorber based on the multilayered HMM pyramids is flexible in terms of bandwidth. However, low melting point metals in HMM pyramids impedes its application potential in high temperature environment. Considering this, a class of particle absorbers named transferable HMM particles is designed to display selective, omnidirectional, and broadband absorption.^[93] The structure is designed as hyperbolic nanotube (HNT) arrays with each tube consisting of aluminum-doped and pure zinc oxide (Figure 12e,f). The measured broadband absorption is higher than 87% from 1200 nm to over 2200 nm with a maximum absorption of 98.1% at 1550 nm. The degeneration of multiple absorption peaks, which results from surface plasmons and lossy hyperbolic modes, causes the broad absorption band. Additionally, the high melting point HNT arrays can be transferred to transparent flexible substrates with broadband absorption in the NIR, which is a benefit for thermophotovoltaics application.

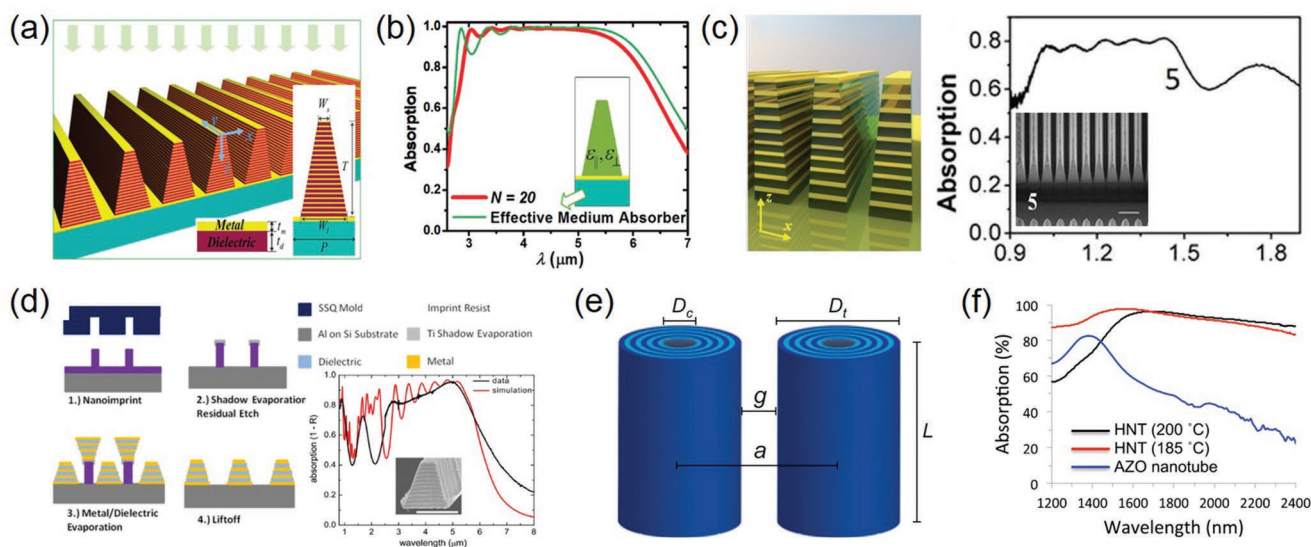


Figure 12. a) Schematic of the anisotropic metamaterial absorber with sawtooth structure. b) Absorptivity for the sawtooth anisotropic metamaterial absorber consisting of 20 layers. Reproduced with permission.^[90] Copyright 2012, American Chemical Society. c) (left) Conceptual illustration of HMM waveguide taper arrays fabricated by FIB. (right) Absorption spectra for the sample with period of 300 nm, top width of 110 nm and bottom width of 270 nm. Reproduced with permission.^[91] Copyright 2013, Springer Nature. d) (left) Technological process for preparation of sawtooth structure using nanoimprint lithography. (right) The absorption spectrum for the sample with period of 700 nm. Reproduced with permission.^[92] Copyright 2014, American Chemical Society. e) Schematic of coupled hyperbolic nanotube arrays. f) Absorption spectra of the hyperbolic nanotube arrays fabricated at the temperatures of 185 and 200 °C. Reproduced with permission.^[93] Copyright 2017, National Academy of Sciences.

3. 2D Planar Hyperbolic Metasurfaces

3.1. Principle of Hyperbolic Metasurfaces

In the aspect of controlling the electromagnetic waves, 3D HMMs have shown great advantages over traditional optical materials due to the unique hyperbolic dispersion characteristics. With further research, it has been found that the drawbacks, such as fabrication complexity in structure and large losses at optical frequencies, greatly limit the application range of bulk HMMs. By compressing complex 3D structures onto 2D surfaces, ultrathin metasurfaces are naturally generated. Because of the capability in fully controlling phase, amplitude, and polarization of light, ultrathin metasurfaces have been used to realize a variety of optical functions such as imaging, holography, and beam shaping.^[143–152] As a planar configuration, the metasurfaces are not only comparable to 3D metamaterials in the manipulation of light, but also have the ability to overcome some of issues of bulk metamaterials, such as lower absorption losses, allowing large-area manufacture and compatible with other existing optoelectronic platforms. As a member of the metasurfaces family, HMSs have extremely large wavevector confinement and PDOS, which make them very promising for the manipulation of in-plane and near-field electromagnetic waves.

Although HMSs can be conceptually obtained by compressing a dimension from 3D bulk HMMs, their principles of electromagnetic responses are not equivalent to each other. Considering the fact that HMSs have been demonstrated in a serial of 2D materials, such as graphene and molybdenum disulfide, it is more accustomed to replace the dielectric constant tensor with the surface conductivity tensor in calculating

the dispersion relation of an infinitesimally homogeneous uniaxial metasurfaces. The conductivity tensor expression is as follows, $\hat{\sigma} = [\sigma_{xx}, 0; 0, \sigma_{yy}]$, where σ_{xx} and σ_{yy} are the x and y components of the conductivity tensor, respectively. Contrary to the case of 3D bulk metamaterials, the uniaxial metasurfaces can simultaneously support the propagation of TM and transverse electric (TE) surface plasmons.^[153–155] However, the difference of dispersion relation between TE surface modes and free space is very small, which means that TE modes are barely confined to the structure surface and thus the related light–matter interaction can be ignored. Therefore, we are more interested in the confined TM surface modes supported by anisotropic metasurface, whose dispersion relation can be given by^[156]

$$\eta_0^2 (k_x^2 \sigma_{xx} + k_y^2 \sigma_{yy})^2 (k_x^2 + k_y^2 - k_0^2) - 4k_0^2 (k_x^2 + k_y^2)^2 = 0 \quad (6)$$

where k_0 is free space wavenumber, k_x and k_y are the x and y components of wavevector of the surface modes, respectively, η_0 is impedance of the free space. Based on this equation, it can be concluded that the band topologies of surface plasmon propagation are determined by the relative signs of the imaginary part of conductivity components $\text{Im}(\sigma_{xx})$ and $\text{Im}(\sigma_{yy})$. For the positive imaginary part of both conductivity component ($\text{Im}(\sigma_{xx}) > 0$, $\text{Im}(\sigma_{yy}) > 0$), the EFC is an elliptic isotropic topology, as shown in Figure 13a, resulting in inductive surface that can allow excited plasmon propagation in all directions within the metasurface sheet. A uniform graphene sheet is a natural example of elliptic isotropic topology.^[157] This special regulatory behavior appears at terahertz and infrared frequencies, which provides an interesting platform to control surface plasmon propagation and enhances light–matter interaction. For negative imaginary part (capacitive surface is

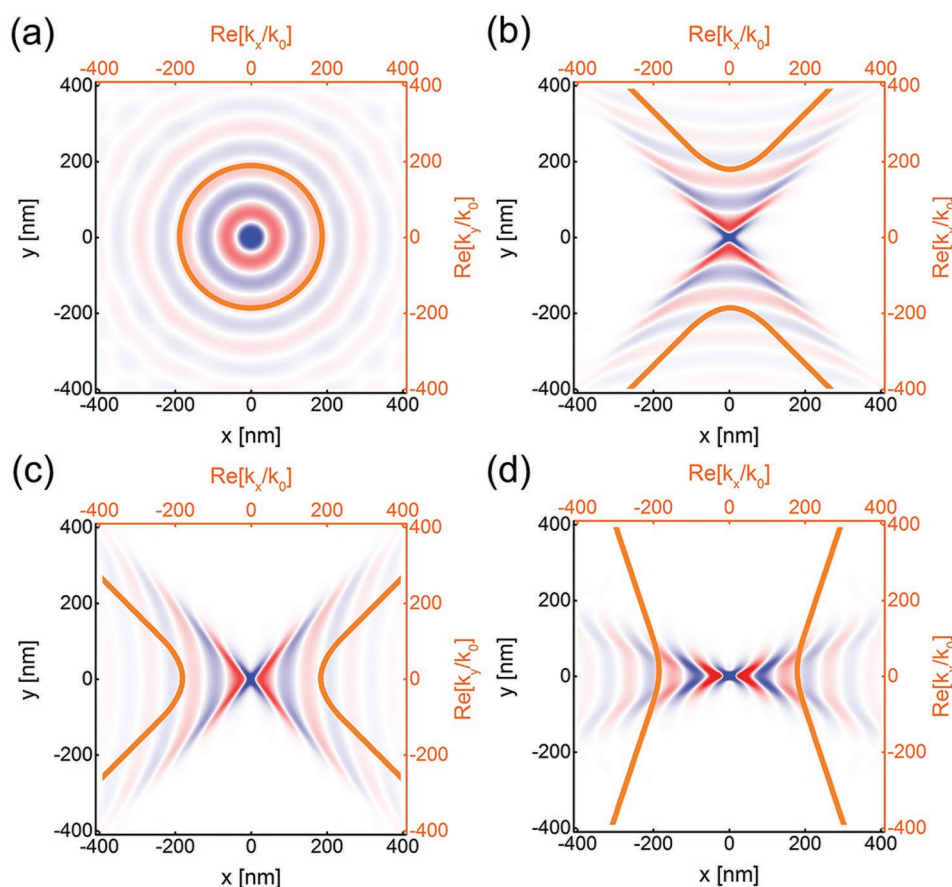


Figure 13. Dispersion relation of uniaxial metasurfaces. Color map is electric field E_z excited by a z-oriented dipole placed about 20 nm above the metasurface. Curve graph is EFC of each metasurface. a) Elliptical metasurface, $\sigma_{xx} = \sigma_{yy} = 1.5 + i20 \mu\text{S}$. b) Hyperbolic metasurface, $\sigma_{xx} = 1.5 - i20 \mu\text{S}$, $\sigma_{yy} = 1.5 + i20 \mu\text{S}$. c) Hyperbolic metasurface, $\sigma_{xx} = 1.5 + i20 \mu\text{S}$, $\sigma_{yy} = 1.5 - i20 \mu\text{S}$. d) σ -near-zero metasurface, $\sigma_{xx} = 1.5 + i20 \mu\text{S}$, $\sigma_{yy} = 1.5 \mu\text{S}$.

equivalent to a dielectric with $\text{Im}(\sigma) < 0$ along one direction and positive imaginary part (inductive surface is equivalent to a metal with $\text{Im}(\sigma) > 0$) along the orthogonal direction, i.e., $\text{Im}(\sigma_{xx})\text{Im}(\sigma_{yy}) < 0$, the surface EFC is a hyperbolic dispersion topology, as shown in Figure 13b,c. In this case, the asymptotic equation of a hyperbolic metasurface can be approximately expressed as^[158]

$$k_y = \pm mk_x \pm b, \text{ with } m = \sqrt{-\sigma_{xx}/\sigma_{yy}}, b = k_0 \sqrt{1 + (2/\eta_0 \sigma_{yy})^2} \quad (7)$$

The bound angle can be given as $\phi = \arctan(\pm \sqrt{-(\sigma_{xx}/\sigma_{yy})})$, which implies that the surface plasmon confinement and propagation direction can be flexibly adjusted by changing the conductivity component of metasurface. In addition, when the EFC evolves from elliptic to hyperbolic geometry, a special transition point will appear for metasurface, which is usually considered as an extremely anisotropic σ -near-zero region. The interesting scenario often requires that the imaginary part of one component of conductivity tensor is much smaller than the other one. As a result, the topology band will be infinitely compressed and be almost flat, which makes surface plasmons propagate toward the direction of smaller imaginary conductivity component and significantly enhances the PDOS (Figure 13d).

3.2. Realizations of Hyperbolic Metasurfaces

To realize hyperbolic EFC of metasurfaces, several possible strategies have been proposed and demonstrated, ranging from use of natural anisotropic materials to construction of artificial anisotropic surfaces. First of all, it is a good choice to start with the natural bulk hyperbolic materials because natural crystals are nonresonant responses to electromagnetic waves and can avoid the complex micro-nanofabrication processes. The most straightforward means to obtain HMS is to reduce the thickness in a particular direction of the bulk hyperbolic materials. Many natural crystals consist of parallel layered structure of atoms, which leads to very weak bonding with van der Waals force between them and can be used to generate hyperbolic surfaces. For example, graphite is a natural hyperbolic material in the ultraviolet band.^[99] In the infrared band, yttrium barium copper oxide and lanthanum strontium copper oxygen exhibit hyperbolic electromagnetic responses.^[99,159] For a long time, the natural hyperbolic material in the most important part of the spectrum, visible range, is missing. This problem is solved by Esslinger et al. with introducing tetradymites, which also is stacked with the atomic monolayer.^[102,103] It is very convenient to realize hyperbolic surfaces by thinning these bulk natural hyperbolic materials to subwavelength scale. Recently, the

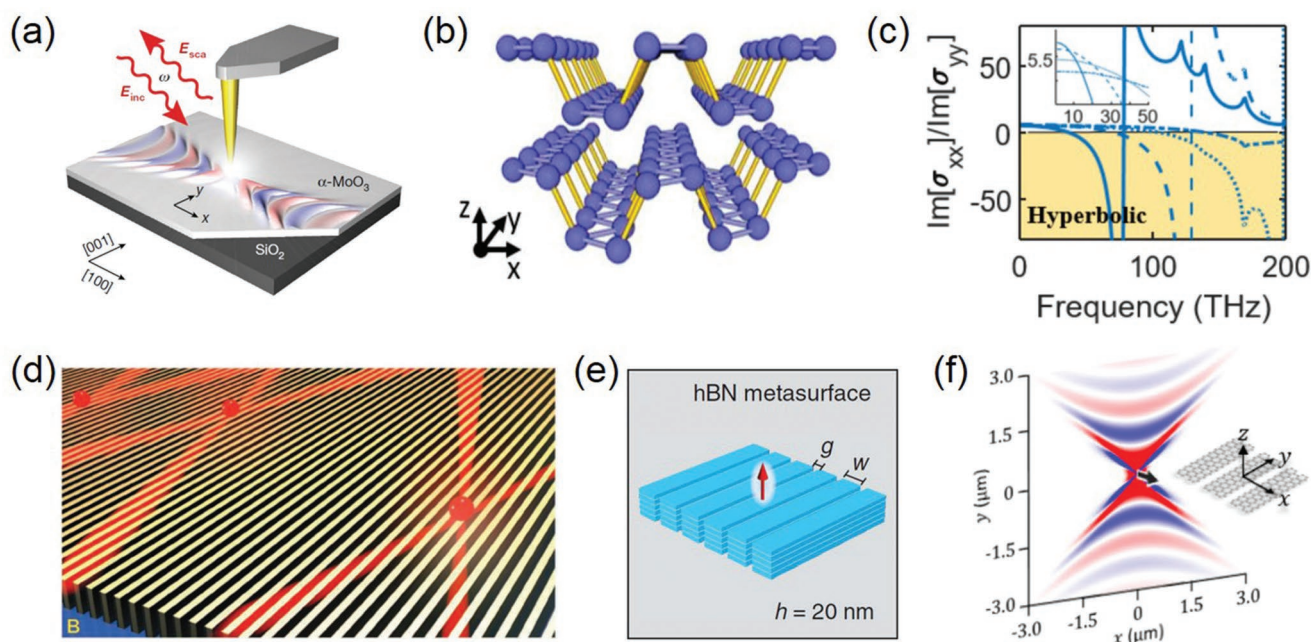


Figure 14. a) Schematic of experimental configuration used to detect in-plane hyperbolic phonon polaritons in α -MoO₃ flake. Reproduced with permission.^[160] Copyright 2018, Springer Nature. b) Lattice structure of a two-layered ultrathin black phosphorus film. c) Anisotropic ratio of the imaginary parts of the conductivity in black phosphorus film. The hyperbolic regime appears at the frequencies where the ratio $\text{Im}(\sigma_{xx})/\text{Im}(\sigma_{yy})$ is negative. Reproduced with permission.^[161] Copyright 2016, IOP Publishing. d) A HMS is made of a subwavelength metallic grating array. Reproduced with permission.^[95] Copyright 2013, American Association for the Advancement of Science. e) Schematic of dipole launching of phonon polaritons on a h-BN HMS. Reproduced with permission.^[167] Copyright 2013, American Association for the Advancement of Science. f) The z-component of surface plasmons excited by a dipole located 10 nm above HMS consisting of a graphene strip array. The inset: schematic of graphene HMS. Reproduced with permission.^[156] Copyright 2015, OSA Publishing.

in-plane elliptic and hyperbolic phonon polaritons (Figure 14a) are verified in long wave infrared region in a thin slab of α -phase molybdenum trioxide (α -MoO₃), a natural van der Waals polar semiconductor.^[160] The highly anisotropic response is mainly due to strong in-plane structural anisotropy, deriving from the different interplanar spacing between the (100) facet and (001) facet. In addition, the black phosphorus (BP) supports the extremely confined anisotropic surface plasmons at mid-IR frequency range.^[161–164] The exotic physical and optical properties mainly result from the extremely anisotropic crystal structure, as shown in Figure 14b. By carefully analyzing the anisotropic conductivity of few layer BP, Figure 14c shows the ratio of the imaginary parts of conductivity component versus frequency for different chemical potentials. The hyperbolic regime appears at the frequencies where the ratio $\text{Im}(\sigma_{xx})/\text{Im}(\sigma_{yy})$ is negative (shaded region).

Besides thinning natural hyperbolic materials, a large number of studies have found that artificial electromagnetic periodic structures on subwavelength scale can also be used to construct artificial HMS, which not only breaks through the limitation of internal crystal structure of natural materials, but also provides unprecedented flexibility for electromagnetic wave regulation. As a practically feasible geometry, 1D periodic gratings have the ability to tailor the in-plane EFC, further controlling the propagation characteristics of surface plasmons at will. A schematic diagram of a typical metal grating metasurface is shown in Figure 14d.^[95] According to the couple mode theory that is usually applied to analyze

the modes interaction in waveguide arrays, the dispersion of surface plasmons at different frequencies can be easily understood and can be drastically modified from concave to convex by changing the structural parameters, such as the height and period. As a result, manipulation of surface plasmons using metallic grating HMS at visible frequency has been demonstrated in theory and experiment.^[165,166] In the mid-infrared region, HMS can be fabricated by lateral structuring thin layers of hexagonal boron nitride (h-BN) into 1D grating,^[167] as shown in Figure 14e. In contrast to metals, h-BN supports strong volume-confined phonon polaritons with much lower losses.^[168] In the Reststrahlen band from 1395 to 1630 cm⁻¹, the in-plane permittivity of h-BN is negative.^[169] Therefore, the artificial periodic grating structure can turn the h-BN thin layer into an in-plane HMS. Besides the metal and van der Waals crystals, 1D grating structure HMS can also be generated by using the 2D materials. As a single layer of atoms, many 2D materials can provide a superior optical performance and are fully compatible with integrated circuits and optoelectronic components. Recently, a simple and effective implementation at terahertz and infrared frequencies has been proposed to realize HMS by using an array of densely packed graphene strips,^[156] as shown in Figure 14f. It shows a hyperbolic topology and allows wave propagation with high field confinement toward the direction defined by the ratio of the conductivity component. Additionally, the principle axis direction and angle of the hyperbolic topology can be manipulated by the graphene chemical potential.

3.3. Applications of Hyperbolic Metasurfaces

3.3.1. Surface Wave Manipulation

An important ability of HMS is to control surface plasmons propagation toward desired directions, including functionalities

such as in-plane beam steering and negative refraction. In 2013, Liu and Zhang first numerically demonstrated that 1D subwavelength metallic grating, a simple metallic metasurface with realistic parameters, has ability to tailor the in-plane dispersion, and can efficiently manipulate surface plasmons in the near-field regime,^[165] as shown in Figure 15a,b. At the

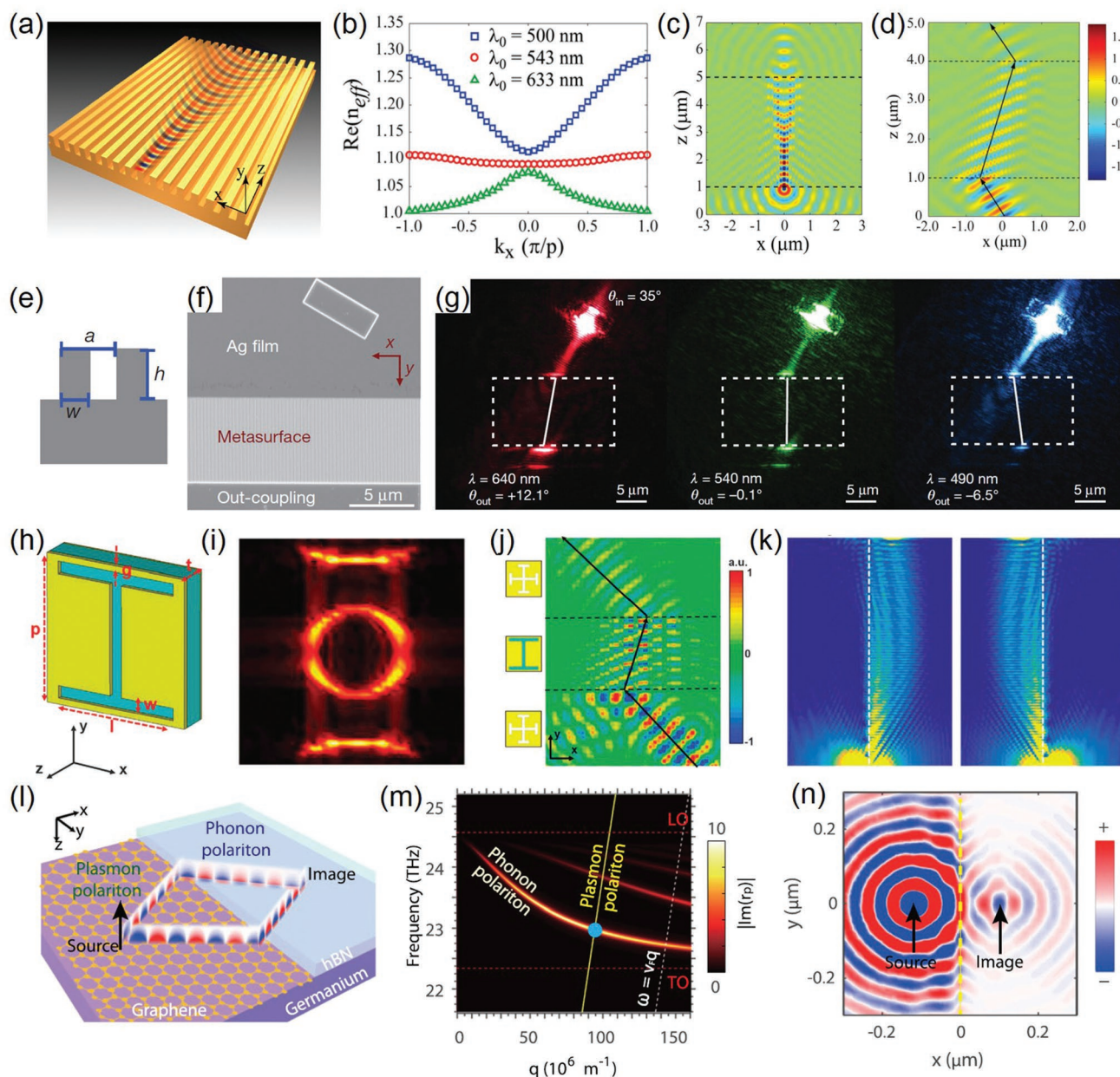


Figure 15. a) Schematic of a HMS consisting of metallic grating arrays. b) Real part of the mode index for surface plasmon at different wavelength with the grating period of 120 nm. c) Propagation of surface plasmon at wavelength of 500 nm, exhibiting anomalous nondivergence. d) Negative refraction of surface plasmon at wavelength of 458 nm. Reproduced with permission.^[165] Copyright 2013, AIP Publishing. e) Schematic of a HMS consisting of Ag grating arrays. f) A SEM image of a device. g) Images of surface plasmon refraction at the interface between uniform Ag and HMS. Dashed boxes indicate the region of HMS. Reproduced with permission.^[166] Copyright 2015, Springer Nature. h) Unit structure of the H-shaped HMS. i) The EFC obtained by taking the Fourier transform of the electric field. j) The electric field distribution shows an in-plane negative refraction at the frequency of 10.5 GHz. k) Electric field intensity distribution of right-handed spin surface plasmon and left-handed spin surface plasmon at 10.5 GHz. Reproduced under the terms of a Creative Commons Attribution 4.0 International License.^[170] Copyright 2017, The Authors. l) Schematic of a structure with a graphene layer attached to a BN slab. m) Dispersion relation of the graphene plasmon polaritons and BN phonon polaritons. n) z-Component of electric field excited by a z-oriented dipole with frequency of 22.96 THz. Reproduced with permission.^[171] Copyright 2017, National Academy of Sciences.

wavelength of 500 nm, the dispersion of coupled plasmon modes on grating metasurface comprises a hyperbolic band. The curvature of plasmon mode dispersion is positive at center and negative at the boundary, denoting the anomalous diffraction of a wave packet. At the wavelength of 600 nm, the EFC is a convex curve, while it becomes flat at wavelength of 543 nm, which corresponds to a nondiffraction propagation of surface plasmons. As a result, the phase front of surface plasmon propagation also is nondivergent at this wavelength, as shown in Figure 15c. In addition, the group velocity, defined as $\nabla_k \omega$, lies normal to the EFC. HMSs hold a negative group velocity, while the traditional flat metal supports a positive one. Therefore, the negative refraction will appear at the interface as the surface plasmon propagating from uniform metal surface to HMSs, which is presented in Figure 15d. The steeper slope of EFC is related to larger grating filling ratio and shorter wavelength and meanwhile indicates all angle negative refraction of surface plasmons in broadband. It is noted that the negative refraction only happens for power flow but wavevector is always positive, meaning a negative group velocity and a positive phase velocity.

The first experimental demonstration of wavelength dependence of surface plasmons based on Ag/air metasurfaces has been reported in 2014.^[166] The HMS is realized on single crystal silver films, which processes mechanical and thermodynamic stability as well as convenience for nanofabrication technics. The schematic and fabricated grating HMS are shown in Figure 15e,f. Below the critical wavelength, the plasmonic modes are strongly confined to the ridges of the grating, which exhibits hyperbolic dispersion. Above the critical wavelength, the modes are only weakly confined, leaving the structure as perturbation and leading to an elliptical dispersion. The negative refraction of surface plasmons is verified with a device consisting of grating structures and a surface plasmon launcher. As a result, as shown in Figure 15g, the propagation direction of surface plasmons changes from normal refraction at $\lambda = 640$ nm to negative refraction at $\lambda = 490$ nm. Around the transition wavelength of 540 nm, the diffraction-free propagation of surface plasmons has been observed in this silver grating HMS. Subsequently, Yang et al. designed another plasmonic HMM supporting surface plasmons propagation at low frequencies.^[170] The unit cell of the surface with complementary H-shaped pattern has a sandwich structure, as shown in Figure 15h. With the capacitances and inductances varying with geometric features, the topology of the EFC can be engineered from an elliptical curve to open hyperbolic one. Figure 15i shows a hyperbolic EFC obtained with applying a spatial Fourier transform of field distributions above the metasurface at 10.5 GHz. The circle at the center corresponds to the vacuum dispersion. The negative refraction of surface plasmons will appear at the interface of background metasurface and HMS at this frequency (Figure 15j). Interestingly, this HMS not only can control the propagation of surface waves, but also can manipulate their transverse spins. When the dispersion curve is hyperbolic, surface waves that propagate along left and right directions, respectively, exhibit left-handed spin and right-handed spin, as shown in Figure 15k, which is contrary to the case for the elliptical dispersion. This phenomenon derives from the spin-orbit coupling and special dispersion curve, and opens up a lot of possibilities for surface wave manipulation.

Besides the structured HMS, in-plane negative refraction and the manipulation of surface plasmon can also be realized in 2D material HMS. For instance, Lin et al. theoretically demonstrated all-angle in-plane negative refraction between graphene plasmon and BN's phonon polariton using graphene-BN heterostructure, which provides an unprecedented control over the dispersion relation.^[171] The heterostructure is shown in Figure 15l, where a graphene layer (left side: allows propagation of plasmon polaritons) is adjacent to a BN slab (right side: allows propagation of phonon polaritons). Figure 15m is the dispersion curve of plasmon polaritons, as depicted in yellow line, and the phonon polaritons as the thick line. The intersection of two dispersion curves is emphasized as the blue circle. The group velocity, defined as $\nabla_q \omega$, lies normal to the EFC. The isotropic dispersion guarantees a positive group velocity for the graphene plasmon polaritons, while it is a negative value for BN phonon polaritons due to the hyperbolic feature of the phonon dispersion. As shown in Figure 15n, when the plasmons propagates from the left graphene region to the right BN region, the all-angle in-plane negative refraction at 22.96 THz occurs due to their opposite signs of group velocities between graphene plasmon and BN's phonon polaritons. Furthermore, the operating frequency of in-plane negative refraction can be easily modulated by changing the chemical potential of graphene.

3.3.2. In-Plane High-Resolution Imaging

By adjusting the geometric parameters of the structure, the concave and flat dispersion relations of surface waves can be obtained in HMS. The corresponding anomalous and diffraction-free propagation of surface waves is very useful for designing metasurface hyperlens, which can be used as a high-resolution in-plane imaging device. A 2D magnifying hyperlens based on an annular multilayer metamaterial is proposed to achieve subwavelength in-plane imaging.^[172] Figure 16a shows the schematic diagram of the metasurface hyperlens, where the concentric rings of PMMA is deposited on a structured gold substrate to form the core structure of the magnifying hyperlens. The objects are placed close to the center of hyperlens and illuminated by the surface plasmons formed by the phase matching structure. According to the surface plasmon dispersion law for the gold/air interface and the gold/PMMA interface, for air (PMMA) interface, the refractive index $n_1(n_2)$ perceived by plasmons is positive (negative). Therefore, the width of the PMMA rings should be chosen as $d_2 = -n_1 d_1 / n_2$, where d_1 is the width of the air rings. All the surface waves in the 2D hyperlens will propagate in the radial direction, which determines the magnification factor. The final magnified images can be obtained with a regular far-field optical microscope. Three PMMA dots are generated around the input surface of the lens with a 0.5 μm periodicity in the radial direction. At the illumination wavelength of 495 nm, the cross-sectional analysis of the plasmon rays shows that the resolution of imaging reaches 70 nm, about $\sim \lambda/7$. Figure 16b is the optical image of the surface imaging process in planar structure, which is obtained from the traditional optical microscope. When the plasmon rays pass through the concentric alternating multilayers, the lateral distance of the three rays will become

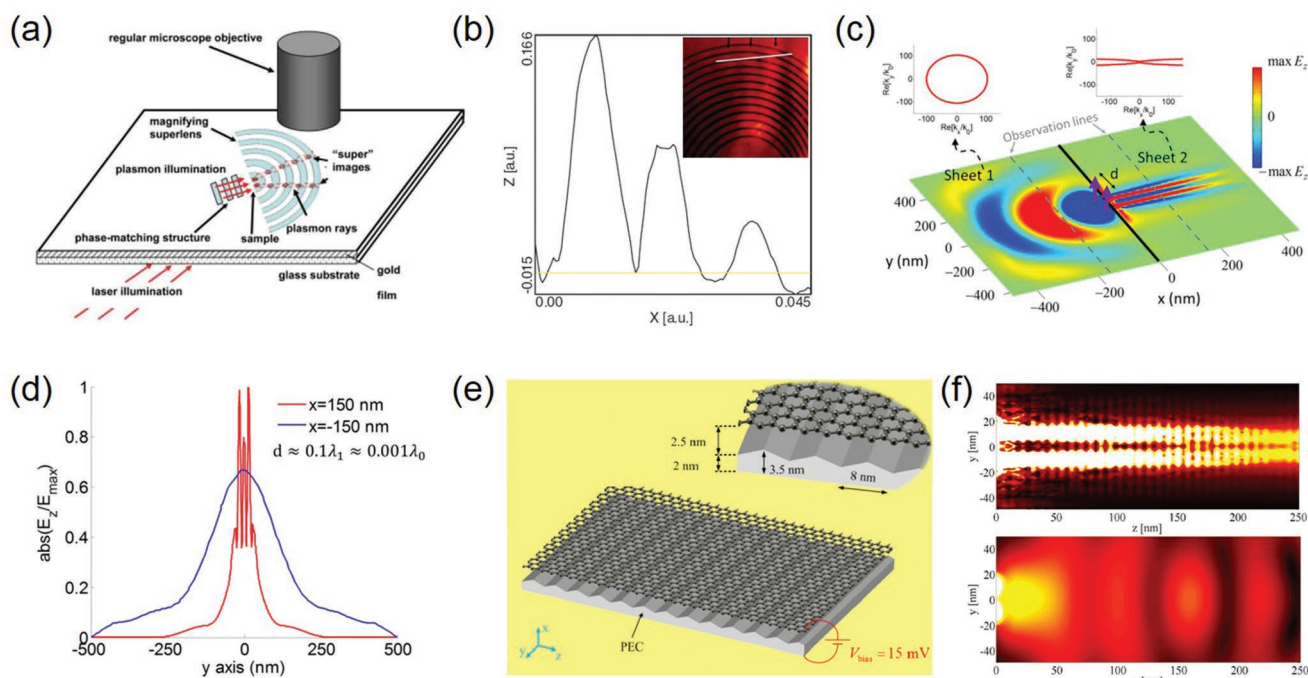


Figure 16. a) Schematic of a planar hyperlens integrated into a traditional far-field optical microscope. b) The cross-section of the electric field intensity along the cutline of inset. Inset: composite image of traditional optical image and the corresponding AFM image. Reproduced with permission.^[172] Copyright 2007, American Association for the Advancement of Science. c) Planar hyperlens. Sheet 1 is excited by two dipoles separated by a distance 60 nm. Insets show the EFC of each sheet. d) Normalized electric field along the two dotted lines marked in the (c). Reproduced with permission.^[98] Copyright 2016, American Chemical Society. e) Triangular ridged substrate for anisotropic conductivity modulation. f) Normalized electric field intensity at the graphene surface with anisotropic conductivity modulation (upper) and the homogenous graphene surface (bottom). Reproduced with permission.^[173] Copyright 2014, American Physical Society.

larger with increasing distance along the radius. Near the outer ring of magnifying hyperlens, the lateral distance of three rays is large enough to be resolved by a traditional far-field optical microscope, indicating that the 2D magnifying hyperlens can be used in-plane super-resolution imaging in the visible frequency range.

In addition to metallic materials, 2D materials, such as graphene, can also be used to prepare the planar hyperlens. Figure 16c shows a graphene hyperlens diagram numerically investigated by Gomez-Diaz and Alu.^[98] The left and right sides of the interface are, respectively, an isotropic metasurface (sheet 1) and anisotropic metasurface (sheet 2). The isotropic metasurface is common graphene sheet, while the anisotropic metasurface can be graphene sheet modulated by closely located corrugated ground planes. In an ideal lossless case, the conductivity tensor components of the metasurface sheet 2 satisfy the condition of $\text{Im}(\sigma_x) \rightarrow \infty$ and $\text{Im}(\sigma_y) \rightarrow 0$. Under such conditions, the component of wavevector k_x is a constant and is independent with the component of wavevector k_y , which suggests that the surface plasmon will propagate toward the x -direction with nondiffraction. In the real simulation model, the conductivity of sheet 1 is $\sigma = 5 \times 10^{-3} + i5 \times 10^{-2}$ mS. The conductivity tensor of sheet 2 is $\sigma_x = 5 \times 10^{-2} + i4$ mS and $\sigma_y = 5 \times 10^{-2} + i4 \times 10^{-8}$ mS. The corresponding EFC is shown at the top of Figure 16c. The graphene metasurface sheet 1 is excited by two dipoles separated by a distance of 60 nm and is placed on the layer 2 nm above the interface of the planar

hyperlens. The designed planar hyperlens can retain the subwavelength information due to the nondiffraction propagation of the plasmons. As shown in Figure 16d, although the distance between the two dipoles is much smaller than the wavelength ($d \approx 0.007\lambda_0$), the detailed information is still well resolved in sheet 2, fully confirming the potential for subwavelength imaging. While, the similar results cannot be achieved in sheet 1 (isotropic graphene layer) due to the diffraction-limited propagation of surface plasmons. Furthermore, Forati et al. proposed a method that convert the isotropic graphene to a hyperbolic metasurface, which will result in a planar 2D hyperlens on graphene.^[173] The design principle is to cling an infinite graphene layer to a substrate of periodic fluctuations, as shown in Figure 16e. A voltage is then applied to the upper and lower surfaces of the structure. Due to the existence of the substrate, different conductivity components will be produced in two directions, and thus the isotropic graphene sheet is transformed into an anisotropic metasurface. By optimizing the parameters of the structure, the diffraction-free propagation of terahertz waves can be realized on the modulated graphene sheet. Figure 16f shows the normalized electric field intensity (E_x) above the modulated graphene layer (top panel) and a uniform graphene layer (bottom panel). These results show that the diffraction effect of the plasmon in uniform graphene can be overcome by the canalization of modulated layer, which confirms the subwavelength imaging capabilities of the planar in-plane hyperlens.

3.3.3. Control over Spontaneous and Thermal Emission

Similar to bulk HMMs, HMS exhibits extremely anisotropic and a hyperbolic EFC, which is closely related to the possibility of unbounded supported plasmon modes and an ideally infinite PDOS, as discussed in the 3D situation. Therefore, the intriguing feature brings the HMS great potential in tailoring the spontaneous emission near the metasurface. In the divergent hyperbolic regime, the Purcell factor can be obtained from the Green function $\hat{G}(r)$ as

$$F_p = \frac{3}{2k^3} n \cdot \int d^3r d^3r' \Phi(r) \Phi(r') \hat{G}(r-r') n \quad (8)$$

where k is the wavenumber, n is the orientation direction vector of the emitter with spatial distribution $\Phi(r)$ and $\hat{G}(r)$ is the dynamic Green function of the structure, which can be evaluated by using 2D Sommerfeld integral.^[174]

The restriction of dissipation and poor coupling in bulk HMMs lowers the efficiency in emission manipulation. However, these limitations can be eliminated in HMS and the efficiency of light-matter interaction enhancement will be further improved. Several works discussing the spontaneous emission engineering using HMS have been reported.^[156,158] For example, in Figure 17a,b, a luminescent HMS exhibits an absorption and emission polarization anisotropy.^[175] The HMS is formed by alternating layers of InGaAsP MQW and silver is

deposited in the trenches between the quantum well pillars. Through the dielectric matrix, the luminescent HMS behaves more like InGaAsP quantum wells with a strong absorption for TM polarization, but resembling silver with a strong scattering for TE polarization. With increasing the optical pumping power, the metasurface exhibits hyperbolic response. The PL enhancement is observed as 3.5 and 1.25 times in the metasurface compared to the control InGaAsP MQW and flat Ag/InGaAsP MQW interface, respectively. In the luminescent HMS, the MQW functions as both emission source and dielectric part, thus the enhancement of light-matter interaction and high-efficient coupling between the plasmon modes are realized simultaneously.

As mentioned above, the uniaxial metasurface can be realized using 2D materials such as graphene and black phosphorus, where the wavenumber contour topology can be tuned with conductivity σ varying under a gate bias.^[176] Figure 17c,d illustrates the spontaneous emission rate of a dipole source oriented along the z -axis with the distance to the BP film and homogeneous graphene sheet with the same chemical potential for both the local and nonlocal models.^[176] Figure 17c corresponds to the elliptical regime where the nonlocality has barely influence on the supported plasmon dispersion. When it changes into hyperbolic as in Figure 17d, the emission rate becomes larger as the emitter is deposited very close to the film, but decays faster as it moves further to the surface. Therefore, the energy coupling efficiency in nonlocal mode can be

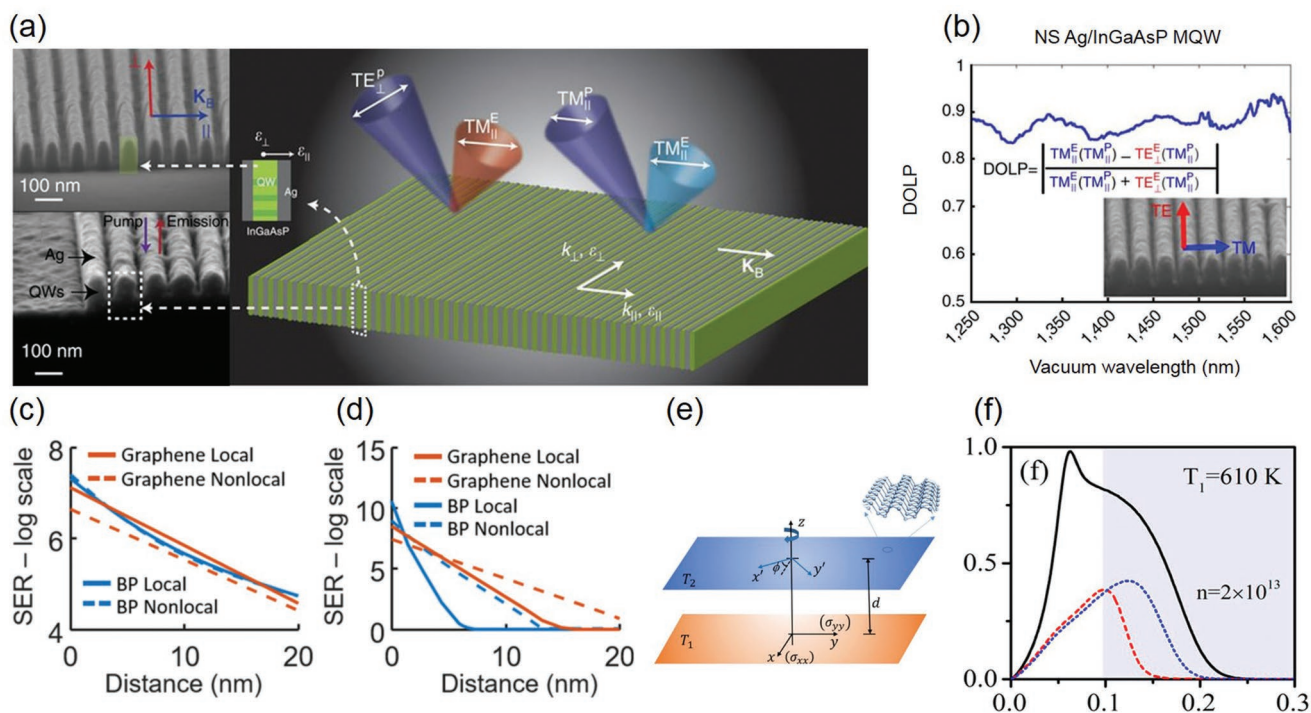


Figure 17. a) SEM images of InGaAsP multiple quantum well pillars and multilayer luminescent HMS as well as the illustration of the pumping ($TM_{||}^P$ or $TE_{||}^P$) and emission polarization parallel ($TM_{||}^E$) to the Bloch vector K_B . b) The degree of linear polarization (DOLP) of emission for parallel-polarized pump. Inset shows SEM of HMSs. Reproduced with permission.^[175] c) Spontaneous emission rate of a z -oriented point source versus its distance to BP thin films and graphene sheets with c) operation frequency $f = 50$ THz, chemical potential $\mu_c = 0.1$ eV and d) $f = 80$ THz, $\mu_c = 0.05$ eV. Reproduced with permission.^[161] e) The radiative heat transfer process between two 2D hyperbolic material with separation distance is d and twisted angle ϕ . f) The radiative heat flux spectrum for concentration of electron n with $2 \times 10^{13} \text{ cm}^{-2}$, while the shaded parts correspond to hyperbolic surface plasmons frequency region. Reproduced with permission.^[178] Copyright 2018, The Authors.

much higher than the local when the dipole is very close to the surface. The electromagnetic properties of BP, graphene, and other 2D hyperbolic materials enable the enhancement of light–matter interaction and wide applications in miniature optoelectronic devices.

The unbounded EFC in HMS can also find applications in thermal emission manipulation.^[80,177–180] The large PDOS of evanescent waves in HMMs can help break the blackbody limit for near-field radiative heat transfer in a broadband frequency range by several orders of magnitude. The relative works using bulk HMMs have been reported,^[71,74] as well as the applications such as near-field thermal imaging^[181] and thermos photovoltaics.^[182] By contrast, HMS performs even better than their 3D counterpart with stronger interaction between the supported plasmon mode with the surrounding. Figure 17e shows the transfer process of radiative heat between two 2D anisotropic material layer, where the electromagnetic energy is radiated from the bottom sheet (temperature T_1) to the upper one (temperature T_2). Figure 17f shows the spectral radiative heat flux for concentration of electron n with $2 \times 10^{13} \text{ cm}^{-2}$, while the high temperature $T_1 = 610 \text{ K}$ and the low temperature $T_2 = T_1 - 10 \text{ K}$ are fixed in different sample groups. The hyperbolic frequency regime is drawn in the shadow region. The enhancement can be over 10^2 to 10^4 times over the blackbody limit, and is contributed to the excitation of anisotropic plasmonic modes and the hyperbolic plasmonic modes. In addition, the thermal modulation can be realized in rotatable 2D hyperbolic material due to the in-plane anisotropy. It should be noted that the enhancement of the heat transfer is greatly affected by the separation distance, as the larger distance will significantly reduce the process due to the evanescent high- k wave in free space. The thermal emission enhancement provides the possible applications of 2D hyperbolic materials in many thermology fields.

4. Fabrications of HMMs and HMSs

As mentioned, artificial 3D HMMs are realized in two common structures, the multilayer and nanowire system. To obtain these nanoscale structures, several fabrication methods are considered. For the multilayer structure, alternating metallic and dielectric thin layers are usually grown by electron-beam physical vapor deposition or magnetron sputtering physical vapor deposition.^[48,50] The characteristic parameters of HMMs are defined by the film thickness. Such technique limits the macroscopic size in one dimension and takes a lot of time. Besides the layer-by-layer grown route, the multilayered HMM can be fabricated by self-rolling technique using strained semiconductor layer.^[54] The system consisted of substrate, a sacrificial layer, a strained semiconductor layer, and a metallic layer sequentially. After removing the sacrificial layer, the strained layer bends up to release strain energy and forms the rolled HMM. The other nanowire system is commonly formed by metal electrodeposition into highly ordered nanoporous anodic alumina oxide (AAO).^[46,59] AAO is synthesized by a two step anodization with the periods and filling ratio tuned in the synthesis procedure. This method is of relatively low-cost and less sensitive to the environment. However, the synthesis

process can introduce impurities and structural imperfections, which may influence the efficiency of HMMs.

The fabrication technique of 2D HMSs is similar to those used in reported metasurfaces. One most common artificial structure is metal/air grating with appropriate feature sizes to support propagating surface plasmons with hyperbolic dispersion. The fabrication process of the hyperbolic grating includes the metal film growth via atomic layer deposition and following e-beam lithography (EBL) with reactive ion etching or FIB milling to define structures.^[175] Compared to the metallic system, thin layers of h-BN can support strongly volume-confined phonon polaritons and is suitable for mid-infrared HMSs.^[105] After the growth of h-BN crystals, mechanical exfoliation using tape is performed to obtain the h-BN flakes. Then, the flakes are re-exfoliated and transferred onto substrate. Finally, the grating structure on h-BN flakes is defined by high-resolution EBL.

The above artificial HMM and HMS structures are designed on the basis of effective medium description. However, it should be noted that, due to the limitation of processing capabilities, the unit size of nanostructures is finitely small, which limits the number of supported wavevectors in real-structured metamaterials. Furthermore, when fabricated unit-cell structures get to extremely small sizes, extra quantum size effect also needs to be taken into account.

5. Conclusion and Outlook

The emerging field of HMMs and metasurfaces with unusual optical properties holds promise to significantly impact nano-optics and photonic technologies. However, we should be clearly aware of that, despite a large amount of theoretical and experimental works proposed and demonstrated, there is still a long way toward the commercialization of hyperbolic technology. The first general limitation is optical absorption losses, which is inherently connected to the plasmonic noble metals, such as silver and gold, used as metamaterial constitutions at optical frequencies. Although these plasmonic metals work very well in the long wavelength infrared, terahertz, and microwave spectral regions, they have high losses originating in part from interband transitions when the incident light shifts to optical frequencies. To address this issue, on the one side, absorption losses can be mitigated by some passive approaches, for example, operating at low metal filling factor for HMMs or exploring alternative low-loss plasmonic materials.^[183] On the other side, research on metamaterials with active properties to completely realize loss compensation recently has emerged at a rapid rate. Active HMMs and metasurfaces consisting of constituent elements with gain and nondissipative properties, such as organic dyes,^[184,185] rare-earth ions,^[186] or quantum well semiconductors,^[187,188] are very promising for creating extremely low-loss or lossless photonic devices.

Besides absorption losses, how to design a HMMs or HMSs with dynamically tunable properties is very important for the real applications.^[175] Although graphene, as a typical terahertz metamaterial constitution, has permittivity tunability by applying external gate voltage to change its Fermi level,^[189,190] convectional plasmonic noble metals always have very large

plasma frequency that cannot be easily adjusted. To realize dynamically tunable HMMs and HMSs at optical frequencies, several attempts are implemented. For example, one can incorporate strong optical nonlinear materials in metamaterials and using Kerr effect from optical excitation pump to tune its permittivity. In addition, employing phase-change materials, such as liquid crystals and transition-metal oxides,^[191–193] are also supported to tune the metamaterial's permittivity by applying some external physical fields. These approaches can enable the controlled or switchable hyperbolic devices.

Moreover, for some hyperbolic applications associated with emission engineering, designing the interface of metamaterials to mediate coupling between propagation waves in free space and the high- k states inside the metamaterials is also very important for extracting the optical information. Tailoring the geometry of the metamaterials^[50] or designing additional structures such as subwavelength gratings or nanoparticles array^[194,195] has been used for energy outcoupling with acceptable efficiencies. In the future, novel coupling mechanisms need to be further studied to achieve high-efficiency energy outcoupling from hyperbolic media.

In conclusion, in this review, we systematically discuss the fundamentals and applications of both HMMs and HMSs. However, currently hyperbolic media are still an active and evolving research area. Therefore, the wide range of potential applications supported by HMMs and HMSs has not been fully explored. For example, one further development is the investigation of heat transfer engineering using hyperbolic media.^[71] The high- k states in HMMs which result in reducing radiative spontaneous emission lifetime can be used for engineering thermal conductivity and thermal emission.^[196] As a result, it is possible to use HMMs to achieve super-Planckian thermal radiation and thermal transfer beyond the blackbody limit at nanoscale.^[74,197–199] Besides thermal engineering, another interesting topic about hyperbolic media is parity-time (PT) symmetry.^[200] The parity and time operators are simultaneously applicable in a PT symmetric system, leading to non-Hermitian systems with purely real spectra.^[201] When light wave is propagating through a PT-symmetric HMM consisting of alternative lossy and gain materials, the wave propagation will exhibit non-reciprocity if both the time-reversal and inversion symmetry of the metamaterial is broken. This would result in a series of extraordinary optical phenomena, such as unidirectional optical transmission and reflection.^[16,202] Other research aspects like fluctuational and macroscopic quantum electrodynamics of hyperbolic media are still at a tentative stage and need significant development.^[203] Overall, the fascinating optical properties and functionalities of HMMs and HMSs open an unprecedented path for the realization of novel metadevices that can find widespread applicability in various photonic systems.

Acknowledgements

P.H. and S.Z. contributed equally to this work. The work was supported in part by the National Key R&D Program of China (Grant No. 2017YFA0303700), the National Natural Science Foundation of China (Grant Nos. 61575092 and 11774163). T.X. acknowledges support from the Fundamental Research Funds for the Central Universities.

Conflict of Interest

The authors declare no conflict of interest.

Keywords

hyperbolic metamaterials, metasurfaces, nanofabrication, optical absorption, optical imaging, optical sensing, surface plasmons

Received: November 22, 2018

Revised: March 13, 2019

Published online: April 16, 2019

- [1] D. R. Smith, J. B. Pendry, M. C. K. Wiltshire, *Science* **2004**, 305, 788.
- [2] N. I. Zheludev, *Science* **2010**, 328, 582.
- [3] C. M. Soukoulis, M. Wegener, *Science* **2010**, 330, 1633.
- [4] C. M. Soukoulis, M. Wegener, *Nat. Photonics* **2011**, 5, 523.
- [5] A. Boltasseva, H. A. Atwater, *Science* **2011**, 331, 290.
- [6] N. I. Zheludev, Y. S. Kivshar, *Nat. Mater.* **2012**, 11, 917.
- [7] V. G. Veselago, *Soviet Phys. – Usp.* **1968**, 10, 509.
- [8] D. R. Smith, W. J. Padilla, D. C. Vier, S. C. Nemat-Nasser, S. Schultz, *Phys. Rev. Lett.* **2000**, 84, 4184.
- [9] R. A. Shelby, D. R. Smith, S. Schultz, *Science* **2001**, 292, 77.
- [10] V. M. Shalaev, *Nat. Photonics* **2007**, 1, 41.
- [11] T. Xu, A. Agrawal, M. Abashin, K. J. Chau, H. J. Lezec, *Nature* **2013**, 497, 470.
- [12] D. R. Smith, P. Kolinko, D. Schurig, *J. Opt. Soc. Am. B* **2004**, 21, 1032.
- [13] Y. Liu, X. Zhang, *Chem. Soc. Rev.* **2011**, 40, 2494.
- [14] A. Poddubny, I. Iorsh, P. Belov, Y. Kivshar, *Nat. Photonics* **2013**, 7, 948.
- [15] L. Ferrari, C. Wu, D. Lepage, X. Zhang, Z. Liu, *Prog. Quantum Electron.* **2015**, 40, 1.
- [16] J. S. T. Smalley, F. Vallini, X. Zhang, Y. Fainman, *Adv. Opt. Photonics* **2018**, 10, 354.
- [17] J. B. Pendry, *Science* **2004**, 306, 1353.
- [18] S. Zhang, Y. S. Park, J. Li, X. C. Lu, W. L. Zhang, X. Zhang, *Phys. Rev. Lett.* **2009**, 102, 023901.
- [19] T. J. Yen, W. J. Padilla, N. Fang, D. C. Vier, D. R. Smith, J. B. Pendry, D. N. Basov, X. Zhang, *Science* **2004**, 303, 1494.
- [20] S. Zhang, W. Fan, B. K. Minhas, A. Frauenglass, K. J. Malloy, S. R. Brueck, *Phys. Rev. Lett.* **2005**, 94, 037402.
- [21] P. A. Belov, *Microwave Opt. Technol. Lett.* **2003**, 37, 259.
- [22] J. Schilling, *Phys. Rev. E* **2006**, 74, 046618.
- [23] A. J. Hoffman, L. Alekseyev, S. S. Howard, K. J. Franz, D. Wasserman, V. A. Podolskiy, E. E. Narimanov, D. L. Sivo, C. Gmachl, *Nat. Mater.* **2007**, 6, 946.
- [24] J. Yao, Z. W. Liu, Y. M. Liu, Y. Wang, C. Sun, G. Bartal, A. M. Stacy, X. Zhang, *Science* **2008**, 321, 930.
- [25] G. V. Naik, J. J. Liu, A. V. Kildishev, V. M. Shalaev, A. Boltasseva, *Proc. Natl. Acad. Sci. USA* **2012**, 109, 8834.
- [26] L. V. Alekseyev, E. E. Narimanov, T. Tumkur, H. Li, Y. A. Barnakov, M. A. Noginov, *Appl. Phys. Lett.* **2010**, 97, 131107.
- [27] T. Xu, H. J. Lezec, *Nat. Commun.* **2014**, 5, 4141.
- [28] P. C. Huo, Y. Z. Liang, S. Zhang, Y. Q. Lu, T. Xu, *Laser Photonics Rev.* **2018**, 12, 1700309.
- [29] Z. Jacob, L. V. Alekseyev, E. Narimanov, *Opt. Express* **2006**, 14, 8247.
- [30] Z. Liu, H. Lee, Y. Xiong, C. Sun, X. Zhang, *Science* **2007**, 315, 1686.
- [31] J. Rho, Z. Ye, Y. Xiong, X. Yin, Z. Liu, H. Choi, G. Bartal, X. Zhang, *Nat. Commun.* **2010**, 1, 143.
- [32] D. L. Lu, Z. W. Liu, *Nat. Commun.* **2012**, 3, 1205.

- [33] J. B. Sun, M. I. Shalae, N. M. Litchinitser, *Nat. Commun.* **2015**, *6*, 7201.
- [34] T. Xu, Y. Zhao, J. Ma, C. Wang, J. Cui, C. Du, X. Luo, *Opt. Express* **2008**, *16*, 13579.
- [35] Y. Xiong, Z. W. Liu, X. Zhang, *Appl. Phys. Lett.* **2008**, *93*, 111116.
- [36] X. Yang, B. Zeng, C. Wang, X. Luo, *Opt. Express* **2009**, *17*, 21560.
- [37] Y. Xiong, Z. Liu, X. Zhang, *Appl. Phys. Lett.* **2009**, *94*, 203108.
- [38] P. Zhu, H. Shi, L. J. Guo, *Opt. Express* **2012**, *20*, 12521.
- [39] S. Ishii, A. V. Kildishev, E. Narimanov, V. M. Shalae, V. P. Drachev, *Laser Photonics Rev.* **2013**, *7*, 265.
- [40] F. Yang, X. Chen, E.-H. Cho, C. S. Lee, P. Jin, L. J. Guo, *Appl. Phys. Express* **2015**, *8*, 062004.
- [41] G. Liang, C. Wang, Z. Zhao, Y. Wang, N. Yao, P. Gao, Y. Luo, G. Gao, Q. Zhao, X. Luo, *Adv. Opt. Mater.* **2015**, *3*, 1248.
- [42] J. Sun, T. Xu, N. M. Litchinitser, *Nano Lett.* **2016**, *16*, 7905.
- [43] L. Liu, P. Gao, K. Liu, W. Kong, Z. Zhao, M. Pu, C. Wang, X. Luo, *Mater. Horiz.* **2017**, *4*, 290.
- [44] X. Chen, C. Zhang, F. Yang, G. Liang, Q. Li, L. J. Guo, *ACS Nano* **2017**, *11*, 9863.
- [45] G. Liang, X. Chen, Q. Zhao, L. J. Guo, *Nanophotonics* **2018**, *7*, 277.
- [46] M. A. Noginov, H. Li, Y. A. Barnakov, D. Dryden, G. Nataraj, G. Zhu, C. E. Bonner, M. Mayy, Z. Jacob, E. E. Narimanov, *Opt. Lett.* **2010**, *35*, 1863.
- [47] T. Tumkur, G. Zhu, P. Black, A. B. Yu, C. E. Bonner, M. A. Noginov, *Appl. Phys. Lett.* **2011**, *99*, 151115.
- [48] H. N. Krishnamoorthy, Z. Jacob, E. Narimanov, I. Kretschmar, V. M. Menon, *Science* **2012**, *336*, 205.
- [49] J. Kim, V. P. Drachev, Z. Jacob, G. V. Naik, A. Boltasseva, E. E. Narimanov, V. M. Shalae, *Opt. Express* **2012**, *20*, 8100.
- [50] D. Lu, J. J. Kan, E. E. Fullerton, Z. Liu, *Nat. Nanotechnol.* **2014**, *9*, 48.
- [51] T. Galfsky, H. N. S. Krishnamoorthy, W. Newman, E. E. Narimanov, Z. Jacob, V. M. Menon, *Optica* **2015**, *2*, 62.
- [52] J. K. Kitur, L. Gu, T. Tumkur, C. Bonner, M. A. Noginov, *ACS Photonics* **2015**, *2*, 1019.
- [53] T. Galfsky, Z. Sun, C. R. Considine, C.-T. Chou, W.-C. Ko, Y.-H. Lee, E. E. Narimanov, V. M. Menon, *Nano Lett.* **2016**, *16*, 4940.
- [54] K. M. Schulz, H. Vu, S. Schwaiger, A. Rottler, T. Korn, D. Sonnenberg, T. Kipp, S. Mendach, *Phys. Rev. Lett.* **2016**, *117*, 085503.
- [55] D. J. Roth, A. V. Krasavin, A. Wade, W. Dickson, A. Murphy, S. Kena-Cohen, R. Pollard, G. A. Wurtz, D. Richards, S. A. Maier, A. V. Zayats, *ACS Photonics* **2017**, *4*, 2513.
- [56] L. Li, W. Wang, T. S. Luk, X. Yang, J. Gao, *ACS Photonics* **2017**, *4*, 501.
- [57] L. Ferrari, J. S. T. Smalley, Y. Fainman, Z. Liu, *Nanoscale* **2017**, *9*, 9034.
- [58] S. Majumder, S. K. Bhadra, *Opt. Commun.* **2017**, *393*, 113.
- [59] P. Ginzburg, D. J. Roth, M. E. Nasir, P. Segovia, A. V. Krasavin, J. Levitt, L. M. Hirvonen, B. Wells, K. Suhling, D. Richards, V. A. Podolskiy, A. V. Zayats, *Light: Sci. Appl.* **2017**, *6*, e16273.
- [60] R. Chandrasekar, Z. Wang, X. Meng, S. I. Azzam, M. Y. Shalaginov, A. Lagutchev, Y. L. Kim, A. Wei, A. V. Kildishev, A. Boltasseva, V. M. Shalae, *ACS Photonics* **2017**, *4*, 674.
- [61] A. F. da Mota, A. Martins, H. Otteyaere, W. Meulebroeck, E. R. Martins, J. Weiner, F. L. Teixeira, B.-H. V. Borges, *ACS Photonics* **2018**, *5*, 1951.
- [62] H.-I. Lin, K.-C. Shen, Y.-M. Liao, Y.-H. Li, P. Perumal, G. Haider, B. H. Cheng, W.-C. Liao, S.-Y. Lin, W.-J. Lin, T.-Y. Lin, Y.-F. Chen, *ACS Photonics* **2018**, *5*, 718.
- [63] K.-C. Shen, C.-T. Ku, C. Hsieh, H.-C. Kuo, Y.-J. Cheng, D. P. Tsai, *Adv. Mater.* **2018**, *30*, 1706918.
- [64] Y. D. Jang, J. S. Baek, V. Devaraj, M. D. Kim, J. D. Song, Y. Wang, X. Zhang, D. Lee, *Optica* **2018**, *5*, 832.
- [65] L. Wang, S. Li, B. Zhang, Y. Qin, Z. Tian, Y. Fang, Y. Li, Z. Liu, Y. Mei, *ACS Appl. Mater. Interfaces* **2018**, *10*, 7704.
- [66] K. J. Lee, Y. U. Lee, S. J. Kim, P. Andre, *Adv. Mater. Interfaces* **2018**, *5*, 1701629.
- [67] D. Lu, H. Qian, K. Wang, H. Shen, F. Wei, Y. Jiang, E. E. Fullerton, P. K. L. Yu, Z. Liu, *Adv. Mater.* **2018**, *30*, 1706411.
- [68] E. E. Narimanov, *Phys. Rev. B* **2018**, *98*, 041401.
- [69] Y. Shen, Y. Yan, A. N. Briggeman, H. Kim, N. C. Giebink, *Nano Lett.* **2018**, *18*, 1693.
- [70] L. Ferrari, D. Lu, D. Lepage, Z. Liu, *Opt. Express* **2014**, *22*, 4301.
- [71] Y. Guo, C. L. Cortes, S. Molesky, Z. Jacob, *Appl. Phys. Lett.* **2012**, *101*, 559.
- [72] S. A. Biehs, M. Tschikin, P. Ben-Abdallah, *Phys. Rev. Lett.* **2012**, *109*, 104301.
- [73] Y. Guo, C. L. Cortes, S. Molesky, Z. Jacob, *Appl. Phys. Lett.* **2012**, *101*, 131106.
- [74] Y. Guo, Z. Jacob, *Opt. Express* **2013**, *21*, 15014.
- [75] S. A. Biehs, M. Tschikin, R. Messina, P. Benabdallah, *Appl. Phys. Lett.* **2013**, *102*, 131106.
- [76] P. N. Dyachenko, S. Molesky, A. Y. Petrov, M. Störmer, T. Krekeler, S. Lang, M. Ritter, Z. Jacob, M. Eich, *Nat. Commun.* **2016**, *7*, 11809.
- [77] S. Campione, F. Marquier, J.-P. Hugonin, A. R. Ellis, J. F. Klem, M. B. Sinclair, T. S. Luk, *Sci. Rep.* **2016**, *6*, 34746.
- [78] R. Deshmukh, S.-A. Biehs, E. Khwaja, T. Galfsky, G. S. Agarwal, V. M. Menon, *ACS Photonics* **2018**, *5*, 2737.
- [79] Y. Zhou, G. Scuri, D. S. Wild, A. A. High, A. Dibos, L. A. Jauregui, C. Shu, K. De Greve, K. Pistunova, A. Y. Joe, T. Taniguchi, K. Watanabe, P. Kim, M. D. Lukin, H. Park, *Nat. Nanotechnol.* **2017**, *12*, 856.
- [80] K.-J. Tielrooij, N. C. Hesp, A. Principi, M. B. Lundeberg, E. A. Pogna, L. Banszerus, Z. Mics, M. Massicotte, P. Schmidt, D. Davydovskaya, *Nat. Nanotechnol.* **2018**, *13*, 41.
- [81] A. V. Kabashin, P. Evans, S. Pastkovsky, W. Hendren, G. A. Wurtz, R. Atkinson, R. Pollard, V. A. Podolskiy, A. V. Zayats, *Nat. Mater.* **2009**, *8*, 867.
- [82] M. E. Nasir, W. Dickson, G. A. Wurtz, W. P. Wardley, A. V. Zayats, *Adv. Mater.* **2014**, *26*, 3532.
- [83] N. Vasilantonakis, G. A. Wurtz, V. A. Podolskiy, A. V. Zayats, *Opt. Express* **2015**, *23*, 14329.
- [84] K. V. Sreekanth, Y. Alapan, M. ElKabbash, E. Ilker, M. Hinczewski, U. A. Gurkan, A. De Luca, G. Strangi, *Nat. Mater.* **2016**, *15*, 621.
- [85] K. V. Sreekanth, Y. Alapan, M. ElKabbash, A. M. Wen, E. Ilker, M. Hinczewski, U. A. Gurkan, N. F. Steinmetz, G. Strangi, *Adv. Opt. Mater.* **2016**, *4*, 1767.
- [86] H. Inan, M. Poyraz, F. Inci, M. A. Lifson, M. Baday, B. T. Cunningham, U. Demirci, *Chem. Soc. Rev.* **2016**, *46*, 366.
- [87] Y. Lee, S. J. Kim, H. Park, B. Lee, *Sensors* **2017**, *17*, 1726.
- [88] K. V. Sreekanth, M. ElKabbash, Y. Alapan, E. I. Ilker, M. Hinczewski, U. A. Gurkan, G. Strangi, *EPJ Appl. Metamater.* **2017**, *4*, 1.
- [89] V. Caligiuri, R. Lento, L. Ricciardi, R. Termine, M. La Deda, S. Siprova, A. Golemme, A. De Luca, *Adv. Opt. Mater.* **2018**, *6*, 1701380.
- [90] Y. Cui, K. H. Fung, J. Xu, H. Ma, Y. Jin, S. He, N. X. Fang, *Nano Lett.* **2012**, *12*, 1443.
- [91] H. Hu, D. Ji, X. Zeng, K. Liu, Q. Gan, *Sci. Rep.* **2013**, *3*, 1249.
- [92] J. Zhou, A. F. Kaplan, L. Chen, L. J. Guo, *ACS Photonics* **2014**, *1*, 618.
- [93] C. T. Riley, J. S. T. Smalley, J. R. J. Brodie, Y. Fainman, D. J. Sirbully, Z. Liu, *Proc. Natl. Acad. Sci. USA* **2017**, *114*, 1264.
- [94] N. Yu, P. Genevet, M. A. Kats, F. Aieta, J. P. Tetienne, F. Capasso, Z. Gaburro, *Science* **2011**, *334*, 333.
- [95] A. V. Kildishev, A. Boltasseva, V. M. Shalae, *Science* **2013**, *339*, 1232009.
- [96] N. Yu, F. Capasso, *Nat. Mater.* **2014**, *13*, 139.

- [97] D. Lin, P. Fan, E. Hasman, M. L. Brongersma, *Science* **2014**, *345*, 298.
- [98] J. S. Gomez-Diaz, A. Alu, *ACS Photonics* **2016**, *3*, 2211.
- [99] J. Sun, N. M. Litchinitser, J. Zhou, *ACS Photonics* **2014**, *1*, 293.
- [100] K. Korzeb, M. Gajc, D. A. Pawlak, *Opt. Express* **2015**, *23*, 25406.
- [101] J. Sun, J. Zhou, B. Li, F. Kang, *Appl. Phys. Lett.* **2011**, *98*, 101901.
- [102] M. Esslinger, R. Vogelgesang, N. Talebi, W. Khunsin, P. Gehring, S. de Zuan, B. Gompf, K. Kern, *ACS Photonics* **2014**, *1*, 1285.
- [103] N. Talebi, C. Ozsoy-Keskinbora, H. M. Benia, K. Kern, C. T. Koch, P. A. van Aken, *ACS Nano* **2016**, *10*, 6988.
- [104] V. P. Drachev, V. A. Podolskiy, A. V. Kildishev, *Opt. Express* **2013**, *21*, 15048.
- [105] M. N. Gjerding, R. Petersen, T. G. Pedersen, N. A. Mortensen, K. S. Thygesen, *Nat. Commun.* **2017**, *8*, 320.
- [106] V. M. Agranovich, V. E. Kravtsov, *Solid State Commun.* **1985**, *55*, 85.
- [107] H. Masuda, K. Fukuda, *Science* **1995**, *268*, 1466.
- [108] K. V. Sreekanth, A. De Luca, G. Strangi, *Sci. Rep.* **2013**, *3*, 3291.
- [109] T. U. Tumkur, L. Gu, J. K. Kitur, E. E. Narimanov, M. A. Noginov, *Appl. Phys. Lett.* **2012**, *100*, 161103.
- [110] X. Yang, J. Yao, J. Rho, X. Yin, X. Zhang, *Nat. Photonics* **2012**, *6*, 450.
- [111] P. R. West, S. Ishii, G. V. Naik, N. K. Emani, V. M. Shalae, A. Boltasseva, *Laser Photonics Rev.* **2010**, *4*, 795.
- [112] M. Y. Shalaginov, V. V. Vorobyov, J. Liu, M. Ferrera, A. V. Akimov, A. Lagutchev, A. N. Smolyaninov, V. V. Klimov, J. Irudayaraj, A. V. Kildishev, A. Boltasseva, V. M. Shalae, *Laser Photonics Rev.* **2015**, *9*, 120.
- [113] D. Korobkin, B. Neuner, C. Fietz, N. Jegenyes, G. Ferro, G. Shvets, *Opt. Express* **2010**, *18*, 22734.
- [114] A. A. Houck, J. B. Brock, I. L. Chuang, *Phys. Rev. Lett.* **2003**, *90*, 137401.
- [115] D. R. Smith, D. Schurig, J. J. Mock, P. Kolinko, P. Rye, *Appl. Phys. Lett.* **2004**, *84*, 2244.
- [116] R. E. Hamam, I. Celanovic, M. Soljačić, *Phys. Rev. A* **2011**, *83*, 035806.
- [117] Y. Shen, D. Ye, I. Celanovic, S. G. Johnson, J. D. Joannopoulos, M. Soljacic, *Science* **2014**, *343*, 1499.
- [118] A. Alu, G. D'Aguanno, N. Mattiucci, M. J. Bloemer, *Phys. Rev. Lett.* **2011**, *106*, 123902.
- [119] C. Argyropoulos, K. Q. Le, N. Mattiucci, G. D'Aguanno, A. Alu, *Phys. Rev. B* **2013**, *87*, 205112.
- [120] E. D. Kosten, J. H. Atwater, J. Parsons, A. Polman, H. A. Atwater, *Light: Sci. Appl.* **2013**, *2*, e45.
- [121] W. S. Cai, D. A. Genov, V. M. Shalae, *Phys. Rev. B* **2005**, *72*, 193101.
- [122] W. T. Lu, S. Sridhar, *Phys. Rev. B* **2008**, *77*, 233101.
- [123] A. V. Kildishev, E. Narimanov, *Opt. Lett.* **2007**, *32*, 3432.
- [124] S. Han, Y. Xiong, D. Genov, Z. Liu, G. Bartal, X. Zhang, *Nano Lett.* **2008**, *8*, 4243.
- [125] V. M. Shalae, *Science* **2008**, *322*, 384.
- [126] W. Wang, H. Xing, L. Fang, Y. Liu, J. Ma, L. Lin, C. Wang, X. Luo, *Opt. Express* **2008**, *16*, 21142.
- [127] Q. Ma, Z. Liu, *Natl. Sci. Rev.* **2018**, *5*, 141.
- [128] E. Narimanov, *ACS Photonics* **2016**, *3*, 1090.
- [129] Q. Ma, H. Qian, S. Montoya, W. Bao, L. Ferrari, H. Hu, E. Khan, Y. Wang, E. E. Fullerton, E. E. Narimanov, X. Zhang, Z. Liu, *ACS Nano* **2018**, *12*, 11316.
- [130] B. Wood, J. B. Pendry, D. P. Tsai, *Phys. Rev. B* **2006**, *74*, 115116.
- [131] E. Khan, E. E. Narimanov, *Appl. Phys. Lett.* **2017**, *111*, 051105.
- [132] Q. Ma, H. Hu, E. Huang, Z. Liu, *Nanoscale* **2017**, *9*, 18268.
- [133] J. P. Dowling, *Found. Phys.* **1993**, *23*, 895.
- [134] E. M. Purcell, in *Confined Electrons and Photons* (Eds: C. Weisbuch, E. Burstein), Springer, Berlin **1995**, p. 839.
- [135] P. Lodahl, A. F. Van Driel, I. S. Nikolaev, A. Irman, K. Overgaag, D. Vanmaekelbergh, W. L. Vos, *Nature* **2004**, *430*, 654.
- [136] K. J. Russell, T.-L. Liu, S. Cui, E. L. Hu, *Nat. Photonics* **2012**, *6*, 459.
- [137] A. Chebykin, A. Orlov, A. Shalin, A. Poddubny, P. Belov, *Phys. Rev. B* **2015**, *91*, 205126.
- [138] A. N. Poddubny, P. A. Belov, Y. S. Kivshar, *Phys. Rev. A* **2011**, *84*, 023807.
- [139] N. I. Landy, S. Sajuyigbe, J. J. Mock, D. R. Smith, W. J. Padilla, *Phys. Rev. Lett.* **2008**, *100*, 207402.
- [140] H. Li, L. H. Yuan, B. Zhou, X. P. Shen, Q. Cheng, T. J. Cui, *J. Appl. Phys.* **2011**, *110*, 014909.
- [141] X. Liu, T. Tyler, T. Starr, A. F. Starr, N. M. Jokerst, W. J. Padilla, *Phys. Rev. Lett.* **2011**, *107*, 045901.
- [142] P. Huo, Y. Liang, S. Zhang, T. Xu, *Opt. Mater. Express* **2017**, *7*, 3591.
- [143] X. Ni, N. K. Emani, A. V. Kildishev, A. Boltasseva, V. M. Shalae, *Science* **2012**, *335*, 427.
- [144] F. Monticone, N. M. Estakhri, A. Alù, *Phys. Rev. Lett.* **2013**, *110*, 203903.
- [145] A. Arbabi, H. Yu, M. Bagheri, A. Faraon, *Nat. Nanotechnol.* **2015**, *10*, 937.
- [146] G. Zheng, H. Muehlenbernd, M. Kenney, G. Li, T. Zentgraf, S. Zhang, *Nat. Nanotechnol.* **2015**, *10*, 308.
- [147] M. Khorasaninejad, W. Chen, R. Devlin, J. Oh, A. Zhu, F. Capasso, *Science* **2016**, *352*, 1190.
- [148] A. Arbabi, E. Arbabi, S. M. Kamali, Y. Horie, S. Han, A. Faraon, *Nat. Commun.* **2016**, *7*, 13682.
- [149] J. P. B. Mueller, N. A. Rubin, R. C. Devlin, B. Groever, F. Capasso, *Phys. Rev. Lett.* **2017**, *118*, 113901.
- [150] R. C. Devlin, A. Ambrosio, N. A. Rubin, J. P. B. Mueller, F. Capasso, *Science* **2017**, *358*, 896.
- [151] W. T. Chen, A. Y. Zhu, V. Sanjeev, M. Khorasaninejad, Z. Shi, E. Lee, F. Capasso, *Nat. Nanotechnol.* **2018**, *13*, 220.
- [152] S. Wang, P. C. Wu, V.-C. Su, Y.-C. Lai, M.-K. Chen, H. Y. Kuo, B. H. Chen, Y. H. Chen, T.-T. Huang, J.-H. Wang, R.-M. Lin, C.-H. Kuan, T. Li, Z. Wang, S. Zhu, D. P. Tsai, *Nat. Nanotechnol.* **2018**, *13*, 227.
- [153] H. J. Bilow, *IEEE Trans. Antennas Propag.* **2003**, *51*, 2788.
- [154] A. M. Patel, A. Grbic, *IEEE Trans. Antennas Propag.* **2013**, *61*, 211.
- [155] R. Quarfoth, D. Sievenpiper, *IEEE Trans. Antennas Propag.* **2013**, *61*, 3597.
- [156] J. S. Gomez-Diaz, M. Tymchenko, A. Alu, *Opt. Mater. Express* **2015**, *5*, 2313.
- [157] F. J. Garcia de Abajo, *ACS Photonics* **2014**, *1*, 135.
- [158] J. S. Gomez-Diaz, M. Tymchenko, A. Alù, *Phys. Rev. Lett.* **2015**, *114*, 233901.
- [159] T. W. Nee, *J. Appl. Phys.* **1992**, *71*, 6002.
- [160] W. Ma, P. Alonso-Gonzalez, S. Li, A. Y. Nikitin, J. Yuan, J. Martin-Sanchez, J. Taboada-Gutierrez, I. Amenabar, P. Li, S. Velez, K. Tolland, Z. Dai, Y. Zhang, S. Sriram, K. Kalantar-Zadeh, S.-T. Lee, R. Hillenbrand, Q. Bao, *Nature* **2018**, *562*, 557.
- [161] D. Correas-Serrano, J. S. Gomez-Diaz, A. Alvarez Melcon, A. Alu, *J. Opt.* **2016**, *18*, 104006.
- [162] Z. Liu, K. Aydin, *Nano Lett.* **2016**, *16*, 3457.
- [163] O. Sancho-Juan, A. Cantarero, G. Martínez-Criado, D. Olguín, N. Garro, A. Cros, M. Salomé, J. Susini, S. Dhar, K. Ploog, *Phys. Rev. Lett.* **2014**, *112*, 176801.
- [164] T. Low, R. Roldan, H. Wang, F. Xia, P. Avouris, L. Martin Moreno, F. Guinea, *Phys. Rev. Lett.* **2014**, *113*, 106802.
- [165] Y. Liu, X. Zhang, *Appl. Phys. Lett.* **2013**, *103*, 141101.
- [166] A. A. High, R. C. Devlin, A. Dibos, M. Polking, D. S. Wild, J. Perczel, N. P. de Leon, M. D. Lukin, H. Park, *Nature* **2015**, *522*, 192.
- [167] P. Li, I. Dolado, F. Javier Alfaro-Mozaz, F. Casanova, L. E. Hueso, S. Liu, J. H. Edgar, A. Y. Nikitin, S. Velez, R. Hillenbrand, *Science* **2018**, *359*, 892.

- [168] J. D. Caldwell, A. V. Kretinin, Y. Chen, V. Giannini, M. M. Fogler, Y. Francescato, C. T. Ellis, J. G. Tischler, C. R. Woods, A. J. Giles, M. Hong, K. Watanabe, T. Taniguchi, S. A. Maier, K. S. Novoselov, *Nat. Commun.* **2014**, *5*, 5221.
- [169] Z. Jacob, *Nat. Mater.* **2014**, *13*, 1081.
- [170] Y. Yang, L. Jing, L. Shen, Z. Wang, B. Zheng, H. Wang, E. Li, N.-H. Shen, T. Koschny, C. M. Soukoulis, H. Chen, *NPG Asia Mater.* **2017**, *9*, e428.
- [171] X. Lin, Y. Yang, N. Rivera, J. J. Lopez, Y. Shen, I. Kaminer, H. Chen, B. Zhang, J. D. Joannopoulos, M. Soljacic, *Proc. Natl. Acad. Sci. USA* **2017**, *114*, 6717.
- [172] I. I. Smolyaninov, Y.-J. Hung, C. C. Davis, *Science* **2007**, *315*, 1699.
- [173] E. Forati, G. W. Hanson, A. B. Yakovlev, A. Alu, *Phys. Rev. B* **2014**, *89*, 081410.
- [174] S. A. H. Gangaraj, T. Low, A. Nemilentsau, G. W. Hanson, *IEEE Trans. Antennas Propag.* **2017**, *65*, 1174.
- [175] J. S. T. Smalley, F. Vallini, S. A. Montoya, L. Ferrari, S. Shahin, C. T. Riley, B. Kanté, E. E. Fullerton, Z. Liu, Y. Fainman, *Nat. Commun.* **2017**, *8*, 13793.
- [176] D. Correias-Serrano, J. S. Gomez-Diaz, M. Tymchenko, A. Alù, *Opt. Express* **2015**, *23*, 29434.
- [177] X. L. Liu, Z. M. Zhang, *Appl. Phys. Lett.* **2015**, *107*, 143114.
- [178] L. Ge, Y. Cang, K. Gong, L. Zhou, D. Yu, Y. Luo, *AIP Adv.* **2018**, *8*, 085321.
- [179] Y. Zhang, H.-L. Yi, H.-P. Tan, *ACS Photonics* **2018**, *5*, 3739.
- [180] I. Trushkov, I. Iorsh, *Phys. Rev. B* **2015**, *92*, 045305.
- [181] Y. De Wilde, F. Formanek, R. Carminati, B. Gralak, P.-A. Lemoine, K. Joulain, J.-P. Mulet, Y. Chen, J.-J. Greffet, *Nature* **2006**, *444*, 740.
- [182] B. Zhao, K. Chen, S. Buddhiraju, G. Bhatt, M. Lipson, S. Fan, *Nano Energy* **2017**, *41*, 344.
- [183] G. V. Naik, V. M. Shalae, A. Boltasseva, *Adv. Mater.* **2013**, *25*, 3264.
- [184] R. S. Savelev, I. V. Shadrivov, P. A. Belov, N. N. Rosanov, S. V. Fedorov, A. A. Sukhorukov, Y. S. Kivshar, *Phys. Rev. B* **2013**, *87*, 115139.
- [185] C. Argyropoulos, N. M. Estakhri, F. Monticone, A. Alu, *Opt. Express* **2013**, *21*, 15037.
- [186] M. Ambati, S. H. Nam, E. Ulin-Avila, D. A. Genov, G. Bartal, X. Zhang, *Nano Lett.* **2008**, *8*, 3998.
- [187] J. Grandidier, G. C. des Francs, S. Massenot, A. Bouhelier, L. Markey, J.-C. Weeber, C. Finot, A. Dereux, *Nano Lett.* **2009**, *9*, 2935.
- [188] B. Kanté, F. Vallini, J. S. T. Smalley, S. Shahin, Y. Fainman, *Opt. Mater. Express* **2015**, *5*, 2300.
- [189] I. V. Iorsh, I. S. Mukhin, I. V. Shadrivov, P. A. Belov, Y. S. Kivshar, *Phys. Rev. B* **2013**, *88*, 039904.
- [190] M. A. K. Othman, C. Guclu, F. Capolino, *Opt. Express* **2013**, *21*, 7614.
- [191] J. Rensberg, S. Zhang, Y. Zhou, A. S. Mcleod, C. Schwarz, M. Goldflam, M. Liu, J. Kerbusch, R. Nawrodt, S. Ramanathan, *Nano Lett.* **2016**, *16*, 1050.
- [192] H. N. S. Krishnamoorthy, Y. Zhou, S. Ramanathan, E. Narimanov, *Appl. Phys. Lett.* **2014**, *104*, 121101.
- [193] T. G. Follan, A. Fali, S. T. White, J. R. Matson, S. Liu, N. A. Aghamiri, J. H. Edgar, R. F. Haglund Jr., Y. Abate, J. D. Caldwell, *Nat. Commun.* **2018**, *9*, 4371.
- [194] K. V. Sreekanth, K. H. Krishna, A. De Luca, G. Strangi, *Sci. Rep.* **2015**, *4*, 6340.
- [195] K. V. Sreekanth, A. De Luca, G. Strangi, *J. Opt.* **2014**, *16*, 105103.
- [196] A. V. Shchegrov, K. Joulain, R. Carminati, J. J. Greffet, *Phys. Rev. Lett.* **2000**, *85*, 1548.
- [197] X. Liu, Z. Zhang, *ACS Photonics* **2015**, *2*, 1320.
- [198] J. Dai, F. Ding, S. I. Bozhevolnyi, M. Yan, *Phys. Rev. B* **2017**, *95*, 245405.
- [199] S. I. Maslovski, C. R. Simovski, S. A. Tretyakov, *New J. Phys.* **2016**, *18*, 013034.
- [200] O. V. Shramkova, G. P. Tsironis, *Phys. Rev. B* **2016**, *94*, 035141.
- [201] C. M. Bender, S. Boettcher, *Phys. Rev. Lett.* **1998**, *80*, 5243.
- [202] A. Leviyev, B. Stein, A. Christofi, T. Galfsky, H. Krishnamoorthy, I. L. Kuskovsky, V. Menon, A. B. Khanikaev, *APL Photonics* **2017**, *2*, 076103.
- [203] A. Davoyan, H. Atwater, *Optica* **2018**, *5*, 608.